Monthly Notices
of the
ROYAL ASTRONOMICAL SOCIETY

MNRAS **482,** 3950–3965 (2019) doi:10.1093/mnras/sty2985
Advance Access publication 2018 November 3

NU Ori: a hierarchical triple system with a strongly magnetic B-type star

M. Shultz,[1,2⋆†] J.-B. Le Bouquin,[3] Th. Rivinius,[4] G. A. Wade,[5] O. Kochukhov,[1] E. Alecian,[3] V. Petit,[2] O. Pfuhl,[6] M. Karl,[6] F. Gao,[6] R. Grellmann,[7] C.-C. Lin,[8] P. Garcia,[3,9,10] S. Lacour[11] and the MiMeS and BinaMIcS Collaborations

[1] *Department of Physics and Astronomy, Uppsala University, Box 516, SE-75120 Uppsala, Sweden*
[2] *Department of Physics and Astronomy, University of Delaware, 217 Sharp Lab, Newark, DE 19716, USA*
[3] *Université Grenoble Alpes, IPAG, F-38000 Grenoble, France*
[4] *ESO – European Organisation for Astronomical Research in the Southern Hemisphere, Casilla 19001, Santiago 19, Chile*
[5] *Department of Physics and Space Science, Royal Military College of Canada, Kingston, Ontario K7K 7B4, Canada*
[6] *Max Planck Institute for Extraterrestrial Physics, Giessenbachstrasse 1, D-85748 Garching, Bayern, Germany*
[7] *Physikalisches Institut der Universität zu Köln, Zülpicher Str 77, D-50397 Köln, Germany*
[8] *Max Planck Institute for Astronomy, Königstuhl 17, D-69117 Heidelberg, Germany*
[9] *Centro de Astrofísica e Gravitação, IST, Universidade de Lisboa, P-1049-001 Lisboa, Portugal*
[10] *Faculdad de Engenharia, Universidade de Porto, rua Dr Roberto Frias, P-4200-465 Porto, Portugal*
[11] *CNRS, IPAG, F-38000 Grenoble, France*

Accepted 2018 October 26. Received 2018 October 10; in original form 2018 August 28

ABSTRACT

NU Ori is a massive spectroscopic and visual binary in the Orion Nebula Cluster, with four components: Aa, Ab, B, and C. The B0.5 primary (Aa) is one of the most massive B-type stars reported to host a magnetic field. We report the detection of a spectroscopic contribution from the C component in high-resolution ESPaDOnS spectra, which is also detected in a Very Large Telescope Interferometer data set. Radial velocity (RV) measurements of the inner binary (designated Aab) yield an orbital period of 14.3027(7) d. The orbit of the third component (designated C) was constrained using both RVs and interferometry. We find C to be on a mildly eccentric 476(1) d orbit. Thanks to spectral disentangling of mean line profiles obtained via least-squares deconvolution, we show that the Zeeman Stokes *V* signature is clearly associated with C, rather than Aa as previously assumed. The physical parameters of the stars were constrained using both orbital and evolutionary models, yielding $M_{\rm Aa} = 14.9 \pm 0.5\,{\rm M}_\odot$, $M_{\rm Ab} = 3.9 \pm 0.7\,{\rm M}_\odot$, and $M_{\rm C} = 7.8 \pm 0.7\,{\rm M}_\odot$. The rotational period obtained from longitudinal magnetic field $\langle B_z \rangle$ measurements is $P_{\rm rot} = 1.09468(7)$ d, consistent with previous results. Modelling of $\langle B_z \rangle$ indicates a surface dipole magnetic field strength of ∼8 kG. NU Ori C has a magnetic field strength, rotational velocity, and luminosity similar to many other stars exhibiting magnetospheric Hα emission, and we find marginal evidence of emission at the expected level (∼1 per cent of the continuum).

Key words: binaries: close – stars: early-type – stars: individual: NU Ori – stars: magnetic field – stars: massive.

1 INTRODUCTION

NU Ori (HD 37061, Brun 747) is the central ionizing B0.5 V star of the M43 H II region of the Orion Nebula Cluster (ONC). The primary is the second hottest B-type star in which a magnetic field has been reported (Petit et al. 2008), after τ Sco (Donati et al. 2006). The system is both a spectroscopic binary, with an orbital period of between 8 and 19 d (Abt, Wang & Cardona 1991; Morrell & Levato 1991), and a visual binary with two companions, one (designated B) detected by high-contrast adaptive optics (Köhler et al. 2006), and a second (designated C) via interferometry (Grellmann et al. 2013).

As a very young, hot star with a magnetic field and a closely orbiting companion, NU Ori is of interest to investigations of the origin of fossil magnetic fields. The rarity of close magnetic binaries (less than 2 per cent of close hot binaries contain a magnetic star; Alecian et al. 2015) has been invoked as supporting evidence by two fossil field formation hypotheses: concentration of primordial magnetic flux within the star-forming environment (in which

⋆ E-mail: mshultz@udel.edu
† Annie Jump Cannon Fellow.

highly magnetized pre-stellar cores inhibit cloud fragmentation; Commerçon, Hennebelle & Henning 2011), or dynamos powered by binary mergers (Schneider et al. 2016). The system is of potential relevance to investigations of the possible contribution of magnetic fields to spin–orbit interactions. Finally, as one of the hottest and most rapidly rotating magnetic early B-type stars known (Petit et al. 2013; Shultz et al. 2018b), it is interesting from the point of view of magnetic wind confinement (e.g. Babel & Montmerle 1997; ud-Doula & Owocki 2002; Townsend & Owocki 2005). In particular, despite its powerful wind and rapid rotation, it shows no sign of magnetospheric emission, thus presenting a potential challenge to theories of magnetosphere formation in early-type stars.

While an orbital period was published by Abt et al. (1991), at that time NU Ori was considered to be an SB1. The spectral contribution of the secondary was first reported by Petit et al. (2008), however, an orbital model making use of the secondary's radial velocities (RVs) has yet to be published. Since the Zeeman Stokes *V* signatures are much wider than the secondary's narrow line profiles, Petit et al. (2008) inferred the broad-lined primary to be the magnetic star. While the surface dipolar magnetic field strength was constrained via Bayesian analysis of the circular polarization profile by Petit et al. (2008), the rotational period of the magnetic star was not known at that time, making a precise magnetic model difficult to determine. Using an expanded spectropolarimetric data set, a rotational period of ∼1.1 d was determined by Shultz et al. (2018b) using longitudinal magnetic field measurements.

Shultz et al. (2017) noted that the primary star of the NU Ori system has stellar and magnetospheric parameters very similar to those of the magnetic β Cep variable ξ^1 CMa, and yet, unlike ξ^1 CMa, shows no sign of magnetospheric emission. The two principal differences between the stars, from a magnetospheric standpoint, are (1) NU Ori's very rapid rotation ($v\sin i \sim 200$ km s^{-1}, $P_{\rm rot} \sim 1.1$ d) as compared to ξ^1 CMa's extremely slow rotation ($P_{\rm rot} \sim 30$ yr), and (2) NU Ori's status as a close binary. At least one star, HD 156324, is known to have a magnetosphere strongly disrupted by orbital dynamics (Shultz et al. 2018a), making it natural to wonder if the failure to detect emission around this star might also be due to the presence of a nearby orbiting companion. This motivates a closer examination of NU Ori's rotational, magnetic, and orbital parameters.

The paper is organized as follows. Observations are described in Section 2. RV measurements, orbital period determination, and orbital modelling are presented in Section 3. Section 4 presents the magnetometry. In Section 5, orbital parameters are used to constrain stellar parameters, which are in turn used with the magnetic and rotational parameters to investigate the star's magnetic, rotational, and magnetospheric properties. The conclusions are summarized in Section 6.

2 OBSERVATIONS

2.1 Spectropolarimetry

ESPaDOnS is a fibre-fed echelle spectropolarimeter mounted at the Canada–France–Hawaii Telescope (CFHT). It has a spectral resolution $\lambda/\Delta\lambda \sim 65\,000$, and a spectral range from 370 to 1050 nm over 40 spectral orders. Each circular polarization observation consists of four polarimetric subexposures, between which the orientation of the instrument's Fresnel rhombs is changed, yielding four intensity (Stokes *I*) spectra, one circularly polarized (Stokes *V*) spectrum, and two null polarization (*N*) spectra (defined by Donati et al. 1997). Wade et al. (2016) described the reduction and analysis of ESPaDOnS data in detail together with the observing strategy of the Magnetism in Massive Stars (MiMeS) Large Programs (LPs).

Table 1. Observation log and radial velocity (RV) measurements. Estimated RV uncertainties are 6 km s^{-1} for Aa, 2 km s^{-1} for Ab, and 9 km s^{-1} for C.

Cal. date	HJD 245 0000	$t_{\rm exp}$ (s)	S/N	RV (Aa) (km s^{-1})	RV (Ab) (km s^{-1})	RV (C) (km s^{-1})
2006-01-12	3747.87907	4 × 800	942	39	53	−11
2006-01-12	3747.92079	4 × 800	923	39	50	−15
2006-01-12	3747.96263	4 × 800	957	41	47	−17
2007-03-08	4167.72958	4 × 800	1066	79	−87	−7
2007-03-08	4167.76959	4 × 800	1081	79	−84	−2
2007-03-08	4167.81034	4 × 800	993	80	−83	−6
2010-01-26	5222.77964	4 × 800	1142	69	−88	−21
2010-01-26	5222.81932	4 × 800	1150	70	−88	−19
2010-02-01	5228.75094	4 × 800	963	19	93	4
2010-02-01	5228.79260	4 × 800	976	19	97	−4
2010-02-02	5229.79356	4 × 800	1130	1	156	4
2010-02-02	5229.83319	4 × 800	1171	1	158	4
2011-11-05	5871.10842	4 × 740	261	15	−30	79
2011-11-06	5872.08868	4 × 740	1017	−1	39	71
2011-11-06	5872.15256	4 × 740	1177	−4	43	71
2011-11-08	5874.06553	4 × 740	111	−33	–	–
2011-11-09	5875.03292	4 × 740	1147	−44	176	75
2012-01-04	5930.71891	4 × 740	967	−32	124	75
2012-01-17	5943.90765	4 × 740	1250	−12	59	80
2012-02-04	5961.75237	4 × 800	1367	−45	180	56
2012-11-26	6257.90822	4 × 700	83	5	–	–
2012-11-26	6257.94322	4 × 700	306	21	33	39
2012-12-05	6266.86057	4 × 700	226	59	−99	30
2012-12-05	6266.90271	4 × 700	605	57	−103	35
2012-12-05	6266.93881	4 × 700	366	57	−103	50
2012-12-22	6283.97259	4 × 700	1182	62	−139	52
2012-12-25	6286.92096	4 × 700	898	5	57	46
2012-12-25	6286.95840	4 × 700	451	6	57	44
2012-12-25	6286.99299	4 × 700	1041	3	59	45
2012-12-28	6289.78387	4 × 700	1087	−33	191	48

The first six observations were acquired in 2006 and 2007, and were reported by Petit et al. (2008).[1] 14 additional Stokes *V* observations were acquired between 2010 January and 2012 February by the MiMeS LP, and a further 10 observations between 2012 November and 2012 December by a PI program.[2] Subexposure times varied between 700 and 800 s; the full exposure time is 4× this duration. The median peak signal-to-noise ratio (S/N) per spectral pixel is 993. Two observations with an S/N ∼ 100 were discarded from the magnetic analysis (although these could still be used to obtain RV measurements for the primary). The observation log is provided in Table 1.

2.2 Interferometry

NU Ori was observed with the PIONIER[3] (Le Bouquin et al. 2011) and GRAVITY[4] (Gravity Collaboration et al. 2017) instruments from the Very Large Telescope Interferometer (VLTI; Mérand et al. 2014). The PIONIER data were reduced and calibrated with the PNDRS package from the JMMC.[5] The GRAVITY data were reduced

[1]Program codes CFHT 05C24 and 07AC10.
[2]Program code CFHT 14AC010.
[3]Program codes 60.A-0209(A), 092.C-0542(A), 094.C-0175(A), 094.C-0397(A), and 096.D-0518(A).
[4]Program code 0100.C-0597(A).
[5]http://www.jmmc.fr/pndrs

Table 2. Interferometric observations of the AC pair. The separation and position angle are the position of the secondary (faintest in H band) with respect to the primary (brightest in H band), measured east (90°) from north (0°). The columns e_{max} and e_{min} are the full width at half-maximum (FWHM) of the major and minor axes of the astrometric error ellipse. The column PA e_{max} is the position angle of the major axis.

Instrument	MJD	Obs. no.	Sep. (mas)	PA (°)	e_{max} (mas)	e_{min} (mas)	PA e_{max} (°)
PIONIER	56601.198	1	8.75	−85.27	0.43	0.35	5
PIONIER	56991.324	2	3.60	−128.41	0.59	0.33	69
PIONIER	56994.236	3	4.04	−124.45	0.20	0.07	152
PIONIER	57007.196	4	5.37	−112.31	0.26	0.10	157
PIONIER	57382.175	5	7.74	+93.01	0.55	0.40	102
PIONIER	57386.128	6	7.51	+93.49	0.74	0.34	5
GRAVITY	58039.3	7	8.543	−82.94	0.02	0.02	5
GRAVITY	58039.4	8	8.549	−82.84	0.02	0.02	5
GRAVITY	58128.1	9	4.39	−37.86	0.02	0.02	5
GRAVITY	58128.1	10	4.40	−37.76	0.02	0.02	5

and calibrated with the ESO package. All observations spatially resolved the C component of the system; the B component was not detected. The GRAVITY data were also reported by Gravity Collaboration, Pfuhl & Karl (2018) in their survey of multiplicity in the ONC. Interferometric observations are summarized in Table 2.

3 MULTIPLICITY

3.1 Radial velocities

Although NU Ori's spectrum is dominated by the hot primary star, it is a known SB2 (Petit et al. 2008), with contributions from a sharp-lined secondary. However, its orbital period is not yet well constrained. We, respectively, designate the primary and secondary as Aa and Ab, following the nomenclature adopted by Grellmann et al. (2013). RVs were measured for the broad-lined primary using the He II 468.6 nm line, which shows no contribution from the secondary. Measurements were obtained by fitting synthetic line profiles convolved with rotational and turbulent broadening using the binary line profile fitting routine described by Grunhut et al. (2017), although for the He II 468.6 nm line only a single stellar component was utilized. These RVs are provided in Table 1. In the process, we also obtained $v\sin i$ and macroturbulent v_{mac} measurements.

Representative spectra in the vicinity of He II 468.6 nm are shown in Fig. 1, where the spectra have been shifted to the rest velocity of the Aa component. He II 468.6 nm shows no intrinsic line profile variability. The same is true for nearby O II lines, which are also expected to be formed solely in the Aa component's photosphere since it should be much hotter than Ab (Aa contributes about 20× as much flux as Ab and has a T_{eff} of ∼30 kK, Simón-Díaz et al. 2011; given the flux ratio, Ab should have an T_{eff} of ∼15 kK, in which O II lines should not form). In contrast, the nearby He I 471.3 nm line shows a complex pattern of line profile variations. This can be partly attributed to the narrow-lined secondary Ab component, however, this star's contribution is not able to fully explain the variability.

Close inspection of the He I lines demonstrated that the line profile variations can be explained by the presence of a third component, which itself has a variable RV. Fig. 2 shows three representative observations of the He I 667.8 nm line, which was selected for analysis as it is both strong and isolated. The B component is approximately 0.47 arcsec from Aa, and the C component is separated by about 0.015 arcsec, thus both would have been within the 1.8 arcsec ESPaDOnS aperture. However, the B component is extremely faint compared to Aa ($\Delta K = 3.23$ mag; Köhler et al. 2006), and so unlikely to contribute much flux. Furthermore, at a distance of ∼400 pc, the B component's projected separation is about 190 au, which would indicate an orbital period of centuries; RV variation on a time-scale of a few years is thus unlikely. We therefore attribute the third spectroscopic component to NU Ori C.

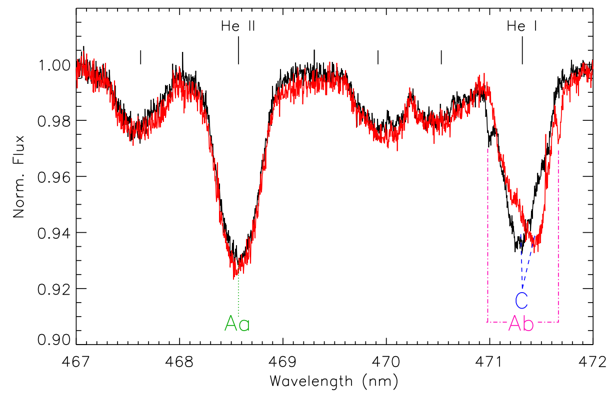

Figure 1. Spectra in the vicinity of the He II 468.6 nm line at maximum radial velocity (RV) separation of the Aab pair. The black spectrum was acquired on 2012 December 22 and the red spectrum on 2012 December 28. Unlabelled lines indicate O II lines. The spectra have been shifted to the rest velocity of the Aa component. There is no line profile variability in He II 468.6 nm. The adjacent He I 471.3 nm line shows a contribution from the Ab component, however, it also shows variation that cannot be attributed to either Aa or Ab. This is due to the contribution of a third star, designated C.

The line can be fit using a three-star model: Aa with $v\sin i = 190 \pm 10\,\mathrm{km\,s^{-1}}$ and $v_{mac} = 100 \pm 20\,\mathrm{km\,s^{-1}}$(see the following paragraph), Ab with $v\sin i = 10 \pm 5\,\mathrm{km\,s^{-1}}$ and $v_{mac} = 5 \pm 5\,\mathrm{km\,s^{-1}}$, and C with $v\sin i = 100 \pm 10\,\mathrm{km\,s^{-1}}$ and $v_{mac} = 5 \pm 5\,\mathrm{km\,s^{-1}}$. The fractional contributions of the best-fitting synthetic line profiles to the total equivalent width are 88 per cent for Aa, 2 per cent for Ab, and 10 per cent for C. RV measurements of Ab and C were obtained from three-component fits to He I 667.8 nm, and are provided in Table 1 (except for two observations for which the S/N was insufficient to clearly distinguish these lines). RV uncertainties were determined statistically, by fitting the same observations using different initial guesses for the full width at half-maximum (FWHM) of the individual components, and taking the standard deviation of the results. Uncertainties are estimated at 6 km s^{-1} for Aa, 2 km s^{-1} for Ab, and 9 km s^{-1} for C.

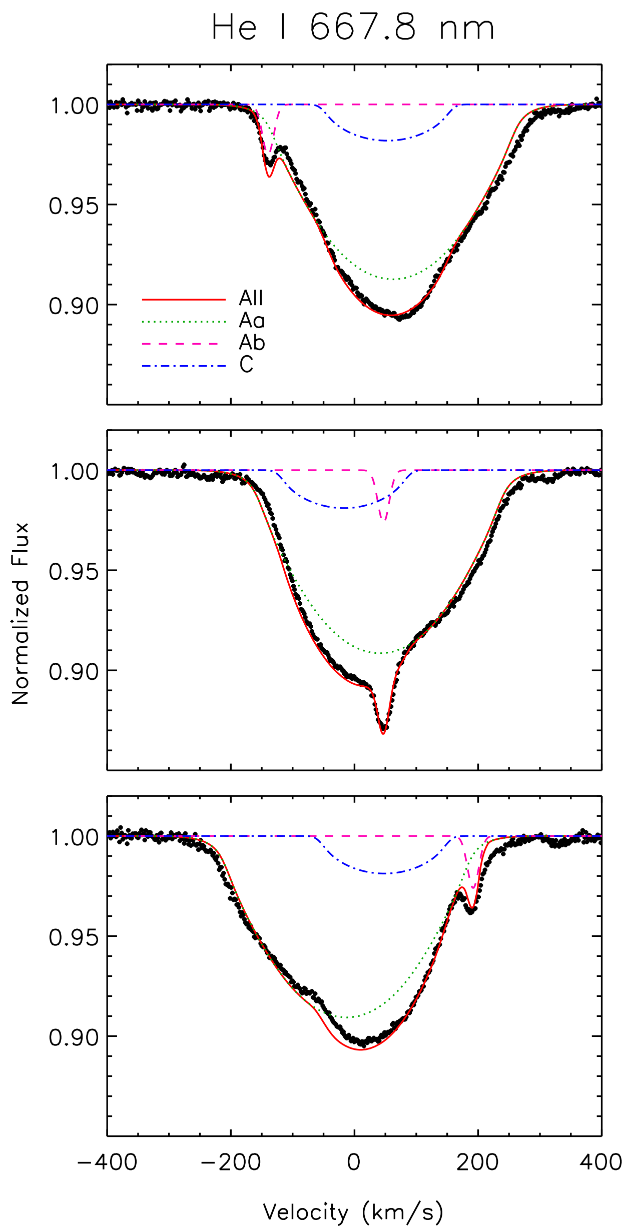

Figure 2. He I 667.8 nm line with a three-component fit at three representative RV separations of the Aab components.

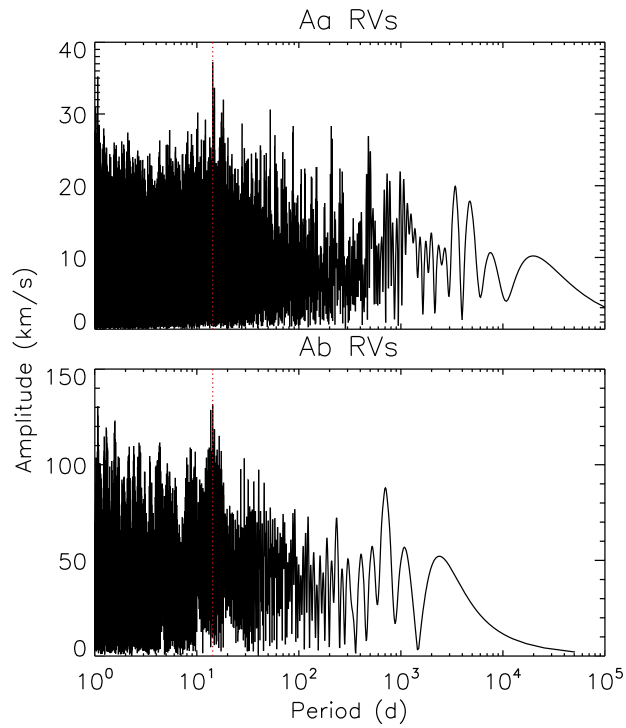

Figure 3. Periodograms for Aa and Ab RVs. The dotted red line indicates the maximum amplitude period.

The macroturbulence determined for Aa is on the high end of the observed distribution for early B-type stars (Simón-Díaz & Herrero 2014; Simón-Díaz et al. 2017). This is likely an artefact of Stark broadening, which was not taken account of in the model. Simón-Díaz & Herrero (2014) found compatible values of both $v\sin i$ and $v_{\rm mac}$ using the Si III 455.3 nm line, however, they used a one-star model and this line exhibits clear variability indicative of a significant contribution from the C component. Using the Si III line, but disentangling the line profiles of the three components as described below in Section 4, we find the same $v\sin i$ but $v_{\rm mac} = 20 \pm 10\,{\rm km\,s^{-1}}$.

3.2 Period analysis

Lomb–Scargle statistics were utilized in order to determine orbital periods from the RV measurements, using PERIOD04 (Lenz & Breger 2005). Periodograms are shown in Fig. 3. Period analysis of the Ab component's RVs (bottom panel of Fig. 3) yields maximum amplitude at 14.305(2) d, where the number in brackets gives the uncertainty in the final digit. The same analysis of the Aa component's He II 468.6 nm RVs yields 14.295(16) d, which is compatible with the result for Ab and is most naturally interpreted to imply that these components are in orbit around one another.

Morrell & Levato (1991) published 10 RV measurements of the Aa component, from which they determined a period of approximately 8 d. Abt et al. (1991) published a further 18 RVs, from which they determined a period of 19.139(3) d. Combining these measurements with our own yields 14.3027(7) d, which is compatible with the value determined from the Ab component's RVs. There is no power at 19 d in the combined periodogram, thus the Abt et al. (1991) period is not supported by our measurements. The Aa and Ab RVs are shown phased with the 14.3027 d period in the top panel of Fig. 5. The amplitude of the Aa RVs is consistent between our measurements and those published by Abt et al. (1991) and Morrell & Levato (1991). As expected given the large difference in flux between Aa and Ab, the RV amplitude of Ab is much greater than that of Aa. There is also a large degree of scatter in the Aab RVs, outside of the formal uncertainties.

The bottom panel of Fig. 4 shows the periodogram obtained for the C component's RVs, which yields a peak at 479(12) d. This is consistent with the lack of RV variation over short time-scales (see Table 1), as well as the lower RV amplitude of the C component as compared to Aab.

To see if the scatter in the Aab RVs may be related to the presence of the C component, residual RVs for Aa and Ab were obtained by fitting sinusoids using

$$\mathrm{RV} = \mathrm{RV}_0 + \mathrm{RV}_1 \sin(\phi + \Phi_0), \qquad (1)$$

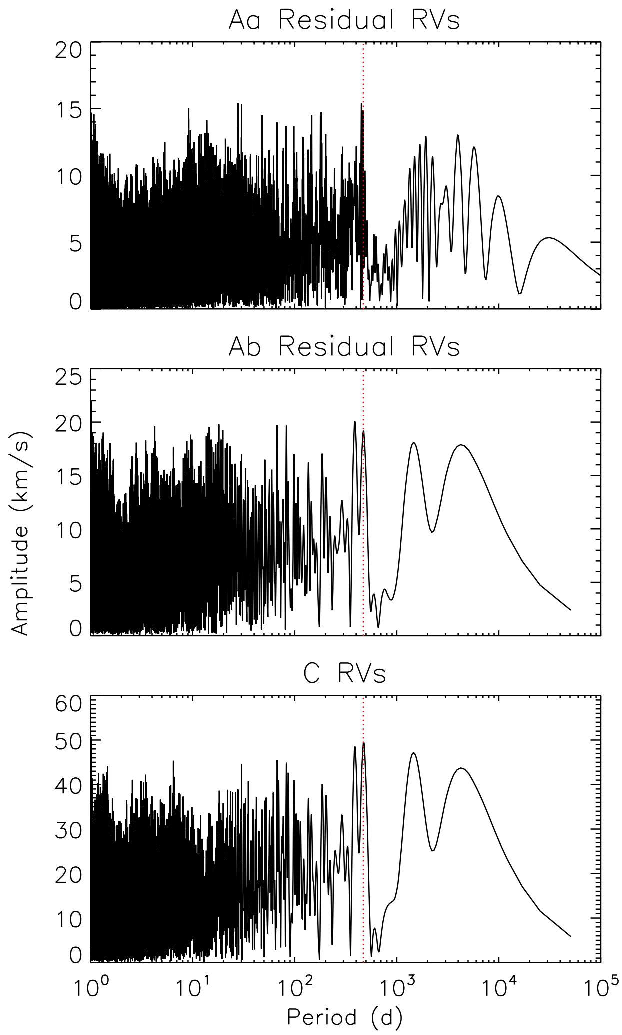

Figure 4. Periodograms for Aa and Ab residual RVs, and C RVs. The dotted red line indicates the most significant period from the Aa and C measurements.

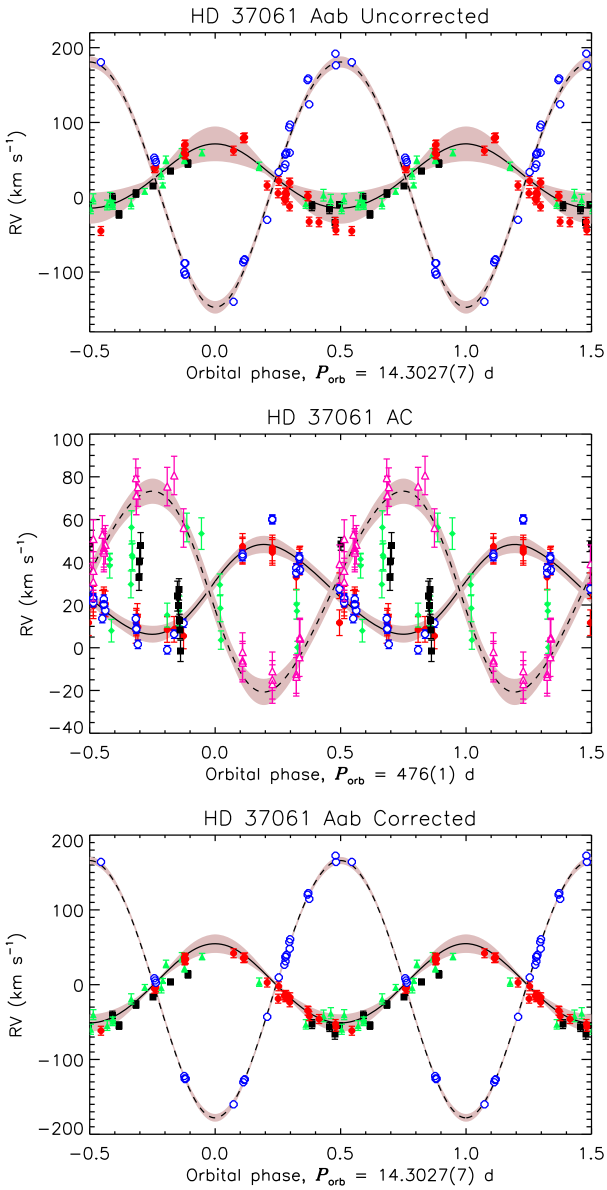

Figure 5. Radial velocity (RV) curves. Open blue circles indicate Ab; filled red circles Aa; filled black squares the Morrell & Levato (1991) measurements; filled green triangles the Abt et al. (1991) measurements; and open purple triangles the C RVs. Top: Aab RVs, folded with the Aab orbital period, without correcting for the AC orbit. Solid (dashed) curves show the best-fitting orbital models for the primary (secondary), shaded regions indicate 1σ uncertainties from Markov chain Monte Carlo (MCMC) modelling. Middle: residual Aab RVs (after removal of orbital variation in top panel), and C RVs, folded with the AC orbital period. Solid and dashed curves are as in the top panel, but for A and C, respectively. Bottom: Aab RVs, corrected for the AC orbit, folded with Aab orbital period. Note that there is substantially less scatter as compared to the top panel.

where ϕ is the orbital phase of the Aab subsystem, and then subtracting the fit from the measurements (leaving out the RV_0 component so as to leave the systemic velocity unchanged). Period analysis of the total residual Aa RVs (top panel of Fig. 4) yields a peak at 469(2) d, consistent with the maximum-amplitude peak in the C RVs; limiting the data set to the ESPaDOnS data yields 484(18) d. Residual Ab RVs yield maximum amplitude at 479(4) d. The interferometric data analysed below (Section 3.4) yield a period of 476.5(1.2) d, with a 468 d period being firmly excluded. Since the shorter period only appears with inclusion of the literature data, it is likely an artefact caused by systematics in the older data set arising from e.g. the contribution of the C component to the RV (which would have affected the Gaussian fits used to measure the RVs).

Residual RVs, and RV measurements of C, are shown phased with the 476 d period in the middle panel of Fig. 5. Residual Aa and Ab RVs vary in phase with one another, in antiphase with the C RVs, and the amplitude of the C RVs is additionally about twice that of the residual Aa and Ab RVs. This further indicates that the 'scatter' in the Aab RVs is a consequence of the orbit of Aab and C about a common centre of mass. The residual literature RVs are not phased coherently with the 476 d period; the quality of the phasing is furthermore not greatly improved by adoption of the 468 d period.

The bottom panel of Fig. 5 shows the Aab RVs after correction for the variation in the Aab subsystem's centre of mass, via subtraction from the RVs of the best-fitting sinusoid to the residual RVs. This correction reduces the scatter in the ESPaDOnS RVs to a magnitude similar to the formal uncertainties.

Table 3. Orbital parameters for the Aab and AC subsystems. For AC, M_1 refers to the mass of the combined Aab subsystem.

Parameter	Aab	AC
P_{orb} (d)	14.3027(7)	476(1)
T_0	244 0578.5(5)	245 3639(7)
v_0 (km s^{-1})	26 ± 6	28 ± 3
K_1 (km s^{-1})	50 ± 8	21 ± 4
K_2 (km s^{-1})	172 ± 3	47 ± 6
e	<0.02	0.09 ± 0.06
ω (°)	–	100 ± 5
M_1/M_2	3.3 ± 0.6	2.2 ± 0.5
$M_1 \sin^3 i$ (M$_\odot$)	12.6 ± 1.2	9.4 ± 3.2
$M_2 \sin^3 i$ (M$_\odot$)	3.5 ± 0.9	4.5 ± 1.4
$(M_1 + M_2)\sin^3 i$ ($\dot{M}$)	16 ± 2	13 ± 5
$a \sin i$ (au)	0.29 ± 0.01	2.8 ± 0.3

3.3 Orbital modelling

For fitting the Aab RVs, the full data set including literature measurements were used, with the RVs corrected for the orbital motion of the C component. For fitting the AC RVs, only the ESPaDOnS data were utilized, since the literature measurements are not phased coherently with the period.

Orbital properties were determined using a Markov chain Monte Carlo (MCMC) algorithm, with the RV semi-amplitudes K_1 and K_2, the systemic velocity v_0, the eccentricity e, the argument of periapsis ω, and the epoch T_0 as free parameters. The initial guess for T_0 is determined via sinusoidal fits to the RVs and residual RVs of the Aa component, with T_0 taken as the time of maximum RV in the cycle immediately preceding the first observation in the time series. The parameter space was explored by 20 independent Markov chains, starting from randomized initial conditions, using a synthetic annealing process that varies the parameter step size for test points by taking it to be the χ^2-weighted standard deviation of the preceding (accepted) test points. The algorithm terminates when the Gelman–Rubin convergence condition is satisfied, i.e. the χ^2 variance within chains is 10 per cent of the variance between chains (Gelman & Rubin 1992). Once the algorithm has converged, fitting parameters and their uncertainties are derived from the peaks and standard deviations of their posterior probability density functions (PDFs). Derived parameters (mass ratios, projected masses, and semimajor axes) were obtained directly from the PDFs of the accepted test points. Mass ratios were obtained from RV semi-amplitudes, and projected masses and semimajor axes were obtained by applying Kepler's laws to the set of accepted test points.

RV curves derived from orbital models are shown in Fig. 5, with the shaded regions indicating the 1σ uncertainties. Orbital model parameters are provided in Table 3. Modelling favours a circular orbit for Aab ($e < 0.02$), and a mildly eccentric orbit for AC ($e = 0.09 \pm 0.06$).

3.4 Results from interferometry

We fit the interferometric observables with a simple binary model, representing the AC pair. The inner pair Aab is largely unresolved even by the longest baseline of VLTI. The remaining free parameters are the separation, the position angle, and the flux ratio between the secondary and the primary. The best fit is considered constant over one photometric band. The best-fitting flux ratios are consistent among the different epochs (0.190 ± 0.015 in *H* band and 0.185 ± 0.011 in *K* band). Inferred positions are summarized in Table 2, and shown in the left-hand panel of Fig. 6.

We simultaneously fit the resolved astrometric positions, the mean Aab residual RVs, and the C RVs. The residual RVs obtained from the literature were discarded as a solution could not be determined using these data. We followed the same convention for the orbital elements as detailed by Le Bouquin et al. (2017). The uncertainties were estimated by fitting an ensemble of input data sets that followed the input mean and uncertainties, and computing the standard deviation of the best-fitting parameters over this ensemble.

The *Gaia* parallax (Gaia Collaboration et al. 2016, 2018)[6] is $\pi = 1.91 \pm 0.04$ mas, implying a distance of 520 ± 10 pc, around 100 pc further than the usual distance from the ONC. Using the *Gaia* distance, the fit returns a mass for the Aab pair of 41 M$_\odot$, i.e. Aa should be an O-type star with $T_{\rm eff} \sim 45$ kK.

Given this implausible result, it seems possible that the *Gaia* astrometry for NU Ori is unreliable, possibly due to the influence of the C component being unaccounted for. Since NU Ori Aa is the central ionizing star of the M43 H II region, it must be physically associated with the ONC. Therefore, we examined the *Gaia* parallaxes of the nine stars within 30 arcsec of NU Ori, under the assumption that these are likely to also be members of the ONC. These are listed in Table 4. The mean and standard deviation for the data set are $d = 390 \pm 80$ pc. One of the sources, a Two Micron All-Sky Survey (2MASS) object, is much further away (590 pc), and is likely a background source; excluding it, the mean and standard deviation are 370 ± 30 pc. This is close to the distance found by Mayne & Naylor (2008) using main-sequence models (390 ± 10 pc), as well as distances to non-thermal ONC sources determined using very long baseline interferometry (VLBI; 390 ± 20 pc, Sandstrom et al. 2007; 388 ± 5 pc, Kounkel 2017). We therefore imposed a distance of 370 ± 30 pc.

The best-fitting orbit using the *Gaia* cluster distance is represented in Fig. 6 and the corresponding orbital elements are summarized in Table 5. The quality of the fit is only marginally improved when removing the constraint on the distance. The $\chi^2_{\rm r}$ decreases from 0.57 to 0.56. The best-fit favours a slightly lower distance (350 ± 18 pc) and masses ($M_{\rm A} = 13.1 \pm 2.5$ M$_\odot$ and $M_{\rm C} = 5.6 \pm 0.8$ M$_\odot$). As can be seen from Table 5, fits utilizing the cluster distance and with distance as a free parameter yield orbital and derived stellar parameters that overlap within uncertainty. The same is not true using the *Gaia* parallax for NU Ori itself. In this case, the derived masses are much higher, due to the much greater RV semi-amplitudes necessary to reconcile the RV curves with the astrometry. The synthetic RV curves obtained using the *Gaia* distance are furthermore a noticeably poorer fit to the measured RVs, again suggesting that the parallax is likely in error. However, the *Gaia* distance solution still yields almost identical values for the eccentricity, the argument of periapsis, the systemic velocity, and the orbital inclination, indicating that these parameters are quite robust against any future revision in the distance.

If we utilize the semimajor axis in astronomical unit (au) obtained from fitting the RVs alone (Table 3), and the orbital inclination and projected semimajor axis in milliarcsec (mas) from the interferometric data, we obtain a distance of 327 ± 41 pc, which is compatible with either the cluster distance or the best-fitting distance where distance is left as a free parameter.

[6]Obtained from http://gea.esac.esa.int/archive/

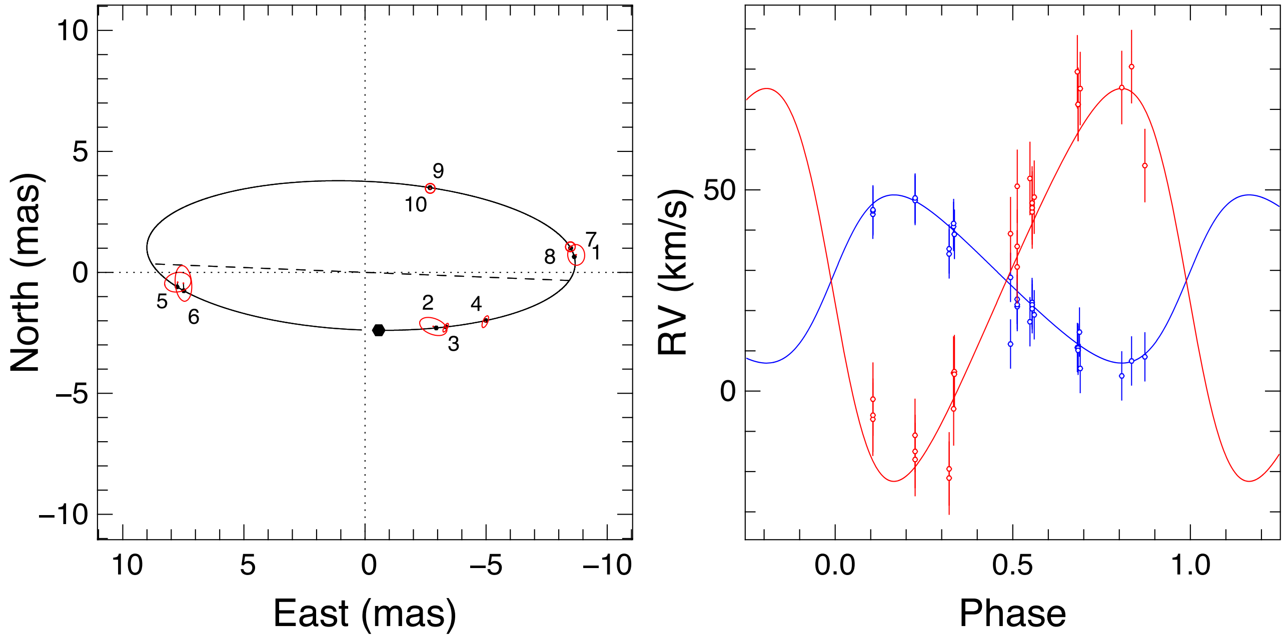

Figure 6. Best-fitting orbital solutions to the astrometric and velocimetric observations, assuming the distance of 370 ± 30 pc. Left: motion of the secondary around the primary. Labels indicate the observation numbers corresponding to Table 2. The periastron of the secondary is represented by a large filled hexagon, and the line of nodes by a dashed line. Small black hexagons indicate the model positions of the C component, red dots indicate the measured positions, and red ellipses indicate the error ellipses. Right: RVs of the primary (blue) and the secondary (red).

Table 4. *Gaia* parallaxes and distances for sources within 30 arcsec of NU Ori (Gaia Collaboration et al. 2016, 2018).

Source	π (mas)	d (pc)
KPM2006 215	2.6 ± 0.1	385 ± 15
KPM2006 216	2.7 ± 0.3	370 ± 40
V* V2509 Ori	3.3 ± 0.2	300 ± 20
KPM2006 219	3.0 ± 0.3	330 ± 20
COUP 1500	2.44 ± 0.06	410 ± 10
KPM2006 220	2.56 ± 0.07	390 ± 10
KPM2006 217	2.6 ± 0.1	385 ± 15
2MASS J05353229 − 0516269	1.7 ± 0.4	590^{+180}_{-110}
V* V1294 Ori	2.66 ± 0.04	370 ± 6

Table 5. Best-fitting orbital parameters for the AC pair considering the interferometric observations and the SB2 RVs, with the distance fixed to the cluster distance inferred from *Gaia* parallaxes (370 ± 30 pc, first column), the distance as a free parameter (second column), and the distance inferred from the *Gaia* parallax of NU Ori (third column).

Parameter	Value	Value	Value
d (pc)	370 ± 30	348 ± 17	524 ± 11
	(fixed, cluster)	(free)	(fixed, *Gaia*)
T_0 (MJD)	53639(7)	53640(8)	53636(12)
$P_{\rm orb}$ (d)	476.5(1.2)	476.5(1.3)	476.8(2.1)
a (mas)	9.06 ± 0.17	9.08 ± 0.14	8.89 ± 0.15
e	0.226 ± 0.025	0.225 ± 0.023	0.227 ± 0.022
Ω (°)	87.7 ± 1.5	87.7 ± 1.2	87.7 ± 1.2
ω (°)	95.4 ± 3.0	95.5 ± 3.0	94.5 ± 4.2
$i_{\rm orb}$ (°)	70.1 ± 0.9	70.2 ± 0.8	69.5 ± 0.8
$K_{\rm A}$ (km s^{-1})	22.5 ± 2.2	20.8 ± 1.6	30.5 ± 1.6
$K_{\rm C}$ (km s^{-1})	52.1 ± 4.1	48.9 ± 2.6	71.6 ± 2.4
v_0 (km s^{-1})	27.5 ± 1.1	27.4 ± 0.9	27.6 ± 0.9
$a_{\rm p}$ (au)	3.38 ± 0.26	3.16 ± 0.20	4.66 ± 0.18
$M_{\rm A}$ (M$_\odot$)	16.2 ± 3.8	13.1 ± 2.5	41.6 ± 3.2
$M_{\rm C}$ (M$_\odot$)	7.0 ± 1.7	5.6 ± 0.8	17.7 ± 1.5
$M_{\rm A}/M_{\rm C}$	2.3 ± 0.2	2.3 ± 0.2	2.4 ± 0.4

The mass obtained for the A component, $M_{\rm A} = 16 \pm 4\,{\rm M}_\odot$, is almost identical to the total projected mass obtained by modelling the Aab RVs, $M_{\rm A}\sin^3 i = 16 \pm 2\,{\rm M}_\odot$. This suggests that the orbital axis of the Aab subsystem must have a similarly large inclination to that obtained for AC.

4 MAGNETOMETRY

As a first step to analysis of NU Ori's magnetic field, least-squares deconvolution (LSD) profiles were extracted using a line mask developed from an extract stellar request from the Vienna Atomic Line Database 3 (VALD3; Piskunov et al. 1995; Ryabchikova et al. 1997, 2015; Kupka et al. 1999, 2000) using the stellar parameters determined for NU Ori Aa ($T_{\rm eff} = 30.5 \pm 0.5$ kK, $\log g = 4.2 \pm 0.1$) by Simón-Díaz et al. (2011). These parameters were selected since Petit et al. (2008) identified the Aa component as the magnetic star, given that the Stokes V signature is much wider than the $v\sin i$ of the secondary component. The line mask was cleaned of all H lines, as well as lines strongly blended with H line wings, lines in spectral regions strongly affected by telluric contamination, lines blended with nebular or interstellar features, and lines in spectral regions affected by ripples. While He lines are often removed due to substantial differences between magnetometry results obtained from He versus metallic lines (e.g. Shultz et al. 2015, 2018b; Yakunin et al. 2015), in this case He lines were left in the mask since the majority of the Stokes V line flux comes from these lines, and the Stokes V profiles extracted using a line mask with He lines excluded did not result in detectable Zeeman signatures. Because of the very high $v\sin i$ of the Aa component, LSD profiles were extracted using

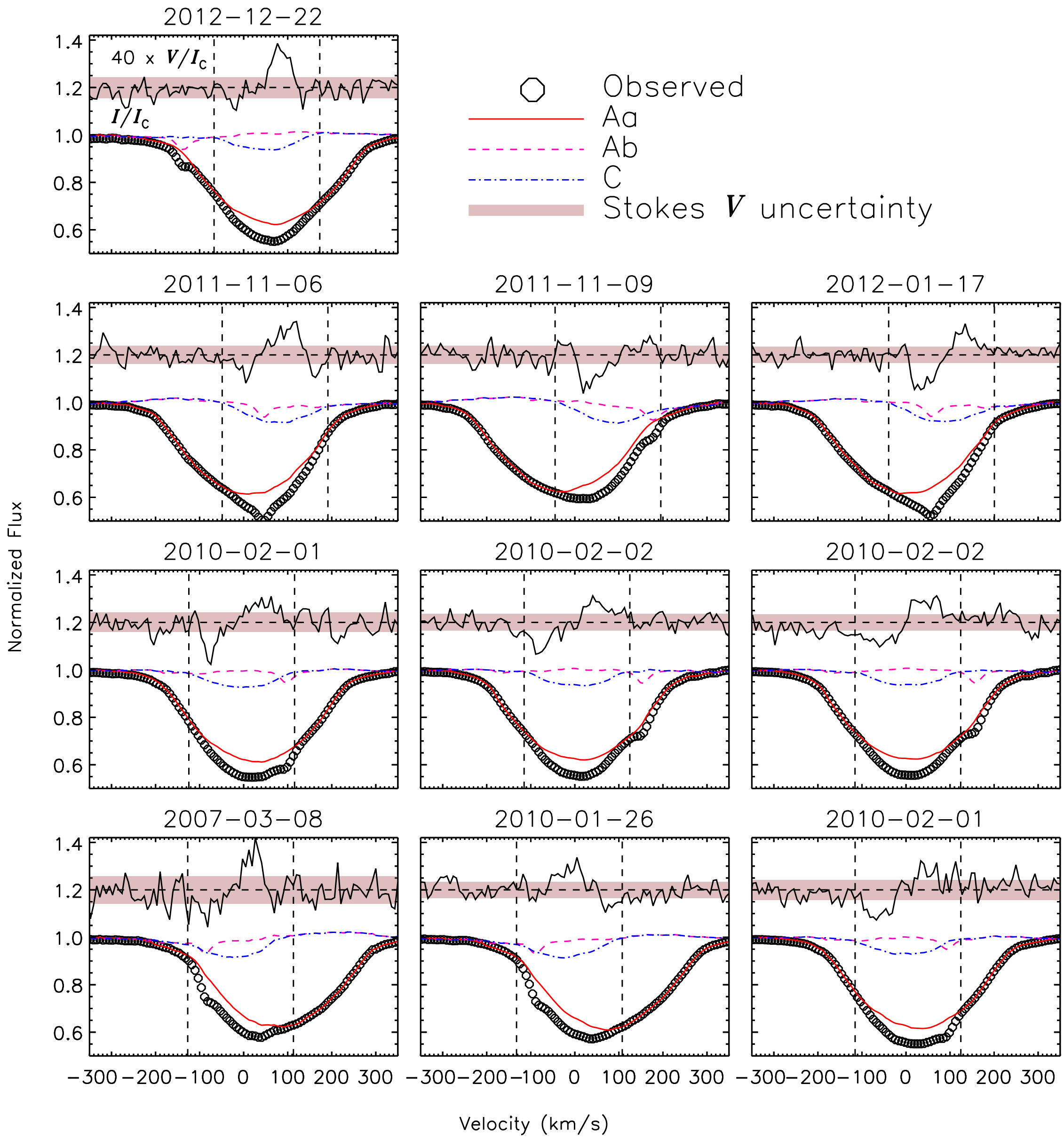

Figure 7. Least-squares deconvolution (LSD) Stokes *I* (bottom) and *V* (top) profiles yielding definite detections. The Stokes *V* continuum is shown by a horizontal dashed line. Vertical dashed lines show the integration ranges for the C component. Note that the Stokes *V* signature is confined within the line profile of the C component in all observations.

a velocity range of $\pm600\,\mathrm{km\,s^{-1}}$ (in order to include enough continuum for normalization) and a velocity pixel size of $7.2\,\mathrm{km\,s^{-1}}$, or four times the average ESPaDOnS velocity pixel (thus raising the per pixel S/N by about a factor of 2). The significance of the signal in Stokes *V* was evaluated using false alarm probabilities (FAPs), with observations classified as definite detections (DDs), marginal detections (MDs), or non-detections (NDs) according to the criteria described by Donati, Semel & Rees (1992) and Donati et al. (1997). Since FAPs essentially evaluate the statistical significance of the Stokes *V* signal inside the stellar line by comparing it to the noise level, they are primarily sensitive to the amplitude of Stokes *V*, which unlike $\langle B_z \rangle$ is not strongly dependent on rotational phase. FAPs are thus a complementary means of checking for the presence of a polarization signal, the principal advantage being that they can detect a magnetic field even at magnetic nulls, i.e. $\langle B_z \rangle = 0$.

Because of the presence of the two companion stars, the LSD profiles were disentangled using an iterative algorithm similar to the one employed by González & Levato (2006). This resulted in the unexpected discovery that it is most likely the C component, rather than the Aa component, that hosts the magnetic field. Fig. 7 shows the 10 LSD profiles yielding DDs in Stokes *V*, with the disentangled Aa, Ab, and C profiles. In all cases the Stokes *V* signature is located entirely inside the line profile of the C component. In some observations, in which the Aa and C components have very different RVs (e.g. 2010 January 26, 2011 November 06, and 2012 January 17), Stokes *V* is clearly offset from the central velocity of Aa. This indicates that the identification of the primary as the magnetic star by Petit et al. (2008) was mistaken.

In an effort to improve the quality of the LSD profiles, a second VALD3 line mask was obtained, this time with stellar parameters

Table 6. $\langle B_z \rangle$ and $\langle N_z \rangle$ measurements. Detection flags for Stokes V (DF_V) or N (DF_N) correspond to definite detections (DD), marginal detections (MD), or non-detections (ND).

	Aa 30 kK, met				Ab 17 kK, met				C 25 kK, met + He			
HJD 245 0000	$\langle B_z \rangle$ (G)	DF_V	$\langle N_z \rangle$ (G)	DF_N	$\langle B_z \rangle$ (G)	DF_V	$\langle N_z \rangle$ (G)	DF_N	$\langle B_z \rangle$ (G)	DF_V	$\langle N_z \rangle$ (G)	DF_N
3747.87907	− 221 ± 253	ND	305 ± 253	ND	− 48 ± 203	ND	161 ± 204	ND	− 122 ± 390	ND	− 378 ± 390	ND
3747.92079	− 113 ± 250	ND	382 ± 250	ND	37 ± 264	ND	− 256 ± 265	ND	316 ± 384	ND	185 ± 384	ND
3747.96263	− 375 ± 231	ND	563 ± 231	ND	− 24 ± 170	ND	42 ± 170	ND	− 200 ± 364	ND	548 ± 364	ND
4167.72958	− 164 ± 230	ND	69 ± 230	ND	69 ± 165	ND	− 37 ± 165	ND	− 1222 ± 340	**DD**	− 11 ± 340	ND
4167.76959	− 250 ± 218	ND	298 ± 218	ND	− 217 ± 160	ND	9 ± 160	ND	− 806 ± 326	ND	830 ± 326	ND
4167.81034	− 252 ± 254	ND	− 77 ± 254	ND	27 ± 137	ND	109 ± 137	ND	− 1641 ± 356	MD	− 90 ± 356	ND
5222.77964	− 254 ± 183	ND	− 3 ± 183	ND	− 210 ± 146	ND	− 1 ± 144	ND	126 ± 196	ND	− 144 ± 196	ND
5222.81932	− 84 ± 182	ND	70 ± 182	ND	− 61 ± 134	ND	− 77 ± 135	ND	538 ± 207	**DD**	298 ± 207	ND
5228.75094	− 250 ± 219	ND	− 43 ± 219	ND	− 70 ± 196	ND	− 357 ± 198	ND	− 2342 ± 305	**DD**	− 377 ± 304	ND
5228.79260	− 193 ± 214	ND	− 267 ± 214	ND	− 159 ± 149	ND	167 ± 149	ND	− 1536 ± 272	**DD**	242 ± 272	ND
5229.79356	− 247 ± 182	ND	− 7 ± 182	ND	55 ± 114	ND	144 ± 114	ND	− 2504 ± 272	**DD**	816 ± 271	ND
5229.83319	− 378 ± 176	ND	− 153 ± 176	ND	206 ± 149	ND	− 4 ± 148	ND	− 2369 ± 268	**DD**	− 2 ± 267	ND
5871.10842	814 ± 1205	ND	− 520 ± 1205	ND	371 ± 1198	ND	− 647 ± 1201	ND	552 ± 1254	ND	1297 ± 1255	ND
5872.08868	− 151 ± 229	ND	596 ± 229	ND	− 7 ± 156	ND	− 204 ± 156	ND	− 135 ± 254	ND	572 ± 254	ND
5872.15256	178 ± 200	ND	− 352 ± 200	ND	− 42 ± 166	ND	− 15 ± 166	ND	− 378 ± 211	**DD**	226 ± 211	ND
5875.03292	− 296 ± 203	ND	164 ± 203	ND	11 ± 137	ND	34 ± 137	ND	− 555 ± 211	**DD**	− 94 ± 211	ND
5930.71891	− 282 ± 263	ND	− 159 ± 263	ND	− 102 ± 200	ND	174 ± 201	ND	− 881 ± 257	ND	90 ± 256	ND
5943.90765	− 34 ± 177	ND	− 41 ± 177	ND	− 22 ± 148	ND	19 ± 148	ND	− 1274 ± 198	**DD**	− 339 ± 198	ND
5961.75237	− 201 ± 169	ND	− 283 ± 169	ND	− 40 ± 153	ND	15 ± 153	ND	324 ± 186	ND	− 85 ± 186	ND
6257.94322	− 234 ± 909	ND	− 1411 ± 910	ND	− 510 ± 617	ND	166 ± 614	ND	− 280 ± 834	ND	− 987 ± 834	ND
6266.86057	2707 ± 6075	ND	452 ± 6075	ND	648 ± 5792	ND	− 1940 ± 5805	ND	11433 ± 5901	ND	3395 ± 5897	ND
6266.90271	121 ± 768	ND	− 546 ± 768	ND	387 ± 455	ND	− 167 ± 454	ND	− 401 ± 1117	ND	361 ± 1117	ND
6266.93881	1093 ± 927	ND	426 ± 927	ND	− 778 ± 688	ND	617 ± 685	ND	353 ± 1300	ND	344 ± 1300	ND
6283.97259	− 119 ± 227	ND	123 ± 227	ND	27 ± 130	ND	− 16 ± 130	ND	− 1245 ± 403	**DD**	− 201 ± 402	ND
6286.92096	83 ± 329	ND	546 ± 329	ND	288 ± 308	ND	− 66 ± 307	ND	− 92 ± 372	ND	370 ± 372	ND
6286.95840	− 214 ± 968	ND	− 633 ± 968	ND	108 ± 903	ND	− 38 ± 903	ND	302 ± 1146	ND	974 ± 1146	ND
6286.99299	18 ± 262	ND	70 ± 262	ND	127 ± 227	ND	− 232 ± 227	ND	197 ± 307	ND	176 ± 307	ND
6289.78387	− 96 ± 263	ND	113 ± 263	ND	− 28 ± 196	ND	299 ± 197	ND	− 1580 ± 319	MD	33 ± 319	ND

closer to those inferred for NU Ori C ($T_{\rm eff} = 24$ kK, $\log g = 4.25$; see Section 5.1). This line mask was cleaned as before, this time with the addition that lines obviously dominated by NU Ori Aa were excluded. Of the 923 lines in the original mask, 483 remained after cleaning. It is these LSD profiles that are shown in Fig. 7. The detection flags obtained for Stokes V and N are summarized in Table 6. Only 10/28 observations yield DDs in Stokes V for NU Ori C; two observations yield MDs; and the remainder are NDs. All N profiles yield NDs, as expected for normal instrument operation.

The longitudinal magnetic field $\langle B_z \rangle$ (Mathys 1989) was evaluated by shifting the disentangled C profiles to their rest velocities, normalizing to the continuum in order for the Stokes I equivalent width to be as accurate as possible, and using an integration range of ± 120 km s^{-1}. $\langle B_z \rangle$ measurements, and the analogous $\langle N_z \rangle$ measurements obtained from the N profiles, are reported in Table 6.

Since the line profiles of the three components are strongly blended in all observations, clean measurements of Aa and Ab are difficult to obtain. In an effort to isolate the contributions of the different stellar components, line masks were prepared using the original 30 kK line mask (for Aa), and a 17 kK line mask (for Ab). In both cases, all He I lines were removed, since C contributes a significant amount of flux to these lines. The line masks were then cleaned to remove any lines with obviously dominant contributions from the other stars. The final line masks contained 111 lines (for the 30 kK mask), and 112 lines (for the 17 kK mask). Examples of the resulting LSD profiles are shown together with the disentangled Stokes I profiles in Fig. 8. Since the metallic lines are typically much weaker than the He lines, the LSD profiles extracted with these masks have much shallower Stokes I profiles than those obtained using the 25 kK metallic+He mask.

The tailored line masks were somewhat successful in reducing the contributions to Stokes I of the other stars, however, in both cases there is still some residual influence. FAPs and $\langle B_z \rangle$ were evaluated from the disentangled profiles using the same method as for those from the 25 kK line mask, with integration ranges appropriate to the star in question (± 220 km s^{-1} for Aa, ± 20 km s^{-1} for Ab). All observations yield NDs in both Stokes V and N. The $\langle B_z \rangle$ measurements obtained from the 30 kK LSD profiles show a systematic bias towards negative values, indicating that the contribution of C to Stokes V was not fully removed. No such bias is apparent in the $\langle B_z \rangle$ measurements from the disentangled LSD profiles of Ab from the 17 kK line mask. This is likely because the much narrower spectral lines of Ab are only blended with those of C at certain observations, unlike those of Aa, which are blended at all times.

4.1 Rotational period

NU Ori's rotational period was previously reported as 1.0950(4) d by Shultz et al. (2018b), however, given the identification of NU Ori C rather than NU Ori Aa as the magnetic star, this should be revisited. Fig. 9 shows the periodogram for NU Ori C's $\langle B_z \rangle$ and $\langle N_z \rangle$ measurements. As expected, there is low amplitude in $\langle N_z \rangle$ at all periods. The $\langle B_z \rangle$ periodogram shows maximum amplitude at 1.09478(7) d, compatible with the period found by Shultz et al.

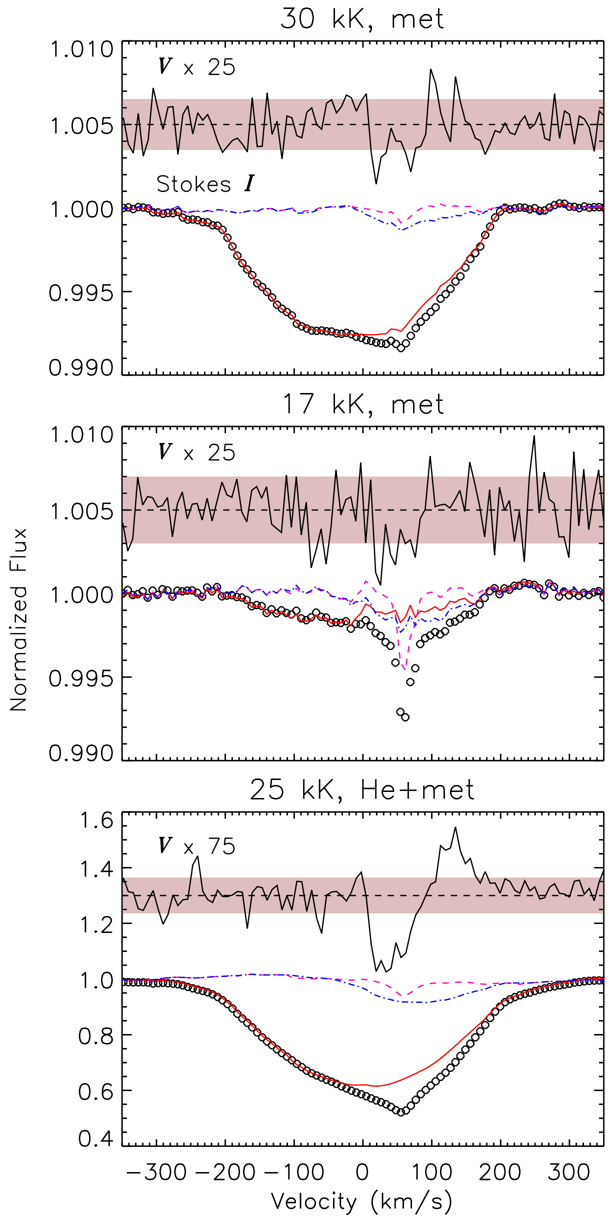

Figure 8. Comparison of LSD profiles extracted using line masks with different effective temperatures customized to emphasize the contribution from one of the three stars: 30 kK, Aa; 17 kK, Ab; 25 kK, C. Extracted and disentangled Stokes *I* profiles are as in Fig. 7. Note that the exclusion of He lines in the 30 and 17 kK line masks leads to much weaker Stokes *I* profiles as compared to those obtained from the 25 kK mask, which includes He lines.

(2018b) albeit at a higher precision. The greater precision is due first to the increased amplitude of the $\langle B_z\rangle$ variation relative to the $\langle B_z\rangle$ uncertainty as compared to the results obtained when Aa was assumed to be the magnetic star, and second to inclusion of the observations reported by Petit et al. (2008) (which were neglected by Shultz et al. 2018b). The FAP of this peak is 0.0005, which is much lower than the $\langle N_z\rangle$ peak (0.21), and lower than the peak of 0.08 in the periodogram reported by Shultz et al. (2018b). This confirms the period found by Shultz et al. (2018b), but at a much higher degree of certainty.

The epoch $T_0 = 245\,3747.5(1)$ was determined by fitting a sinusoid to the data and determining the time of $|\langle B_z\rangle|_{\max}$ in the cycle immediately preceding the first observation. $\langle B_z\rangle$ is shown phased with this ephemeris in Fig. 10. For the purposes of modelling the star's magnetic dipole, a sinusoidal fit was performed using the relation

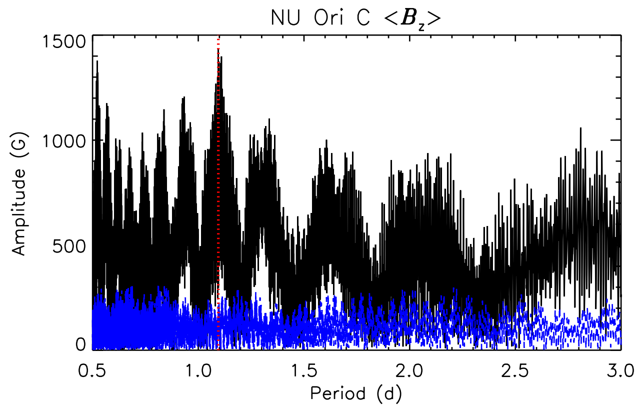

Figure 9. Periodogram for NU Ori C $\langle B_z\rangle$ measurements (solid black) and $\langle N_z\rangle$ measurements (dashed blue). The dotted red line indicates the maximum amplitude period.

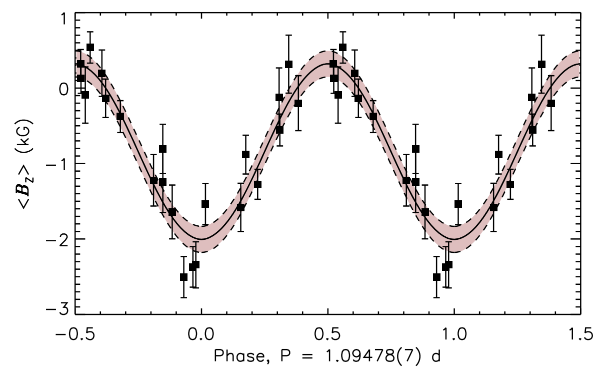

Figure 10. $\langle B_z\rangle$ measurements of the NU Ori C from disentangled LSD profiles, folded with the rotational period. The solid line shows the best-fitting first-order sinusoid, and the grey shaded regions indicate the 1σ uncertainty in the fit.

$$\langle B_z\rangle = B_0 + B_1 \sin(\phi + B_2), \qquad (2)$$

where ϕ is the rotational phase and B_2 is a phase offset. The fit and its uncertainties are shown in Fig. 10. The resulting coefficients are $B_0 = -0.85 \pm 0.07$ kG and $B_1 = 1.18 \pm 0.09$ kG. The reduced χ^2 of the fit is 1.6. Fitting $\langle B_z\rangle$ with the second harmonic yielded a reduced χ^2 of 1.7, i.e. the fit is not improved, indicating that the star's $\langle B_z\rangle$ variation is adequately described by a dipole. If the fit to $\langle B_z\rangle$ had been improved by addition of a second harmonic, a more likely explanation than a multipolar field would be that the contributions of Aa and Ab had been inadequately removed; since a second harmonic is unnecessary, this also suggests that the disentangling procedure was successful in isolating the components.

5 DISCUSSION

5.1 Stellar parameters

To obtain stellar parameters for the system components, a Monte Carlo algorithm was used similar to that described by Pablo et al. (in preparation). The algorithm works by populating the $T_{\rm eff}$–$\log g$

diagram with test points drawn from Gaussian distributions in $T_{\rm eff}$ and log *g*, interpolating stellar parameters via evolutionary models and the orbital relationships of the components, and rejecting points that are inconsistent with known observables. Probability density maps for the three components are shown in Fig. 11 on the $T_{\rm eff}$–log *g* plane, the HRD, and the R_*–M_* plane, and the derived physical parameters are listed in Table 7.

Since the physical parameters of the Ab and C components are difficult to constrain directly from the spectrum, which is dominated by the Aa component, these were fixed using the mass ratios from Table 3, following the assumption that close binaries are primordial and, hence, the stars must be coeval (Bonnell & Bate 1994). The evolutionary models of Ekström et al. (2012), including the effects of rotation, were utilized to determine ages and masses. Test points were accepted if they resulted in (1) projected masses $M_{\rm A}\sin^3 i$ and $M_{\rm C}\sin^3 i$ consistent with the inclination $i_{\rm orb} = 70\overset{\circ}{.}1 \pm 0\overset{\circ}{.}9$ determined from interferometric modelling (Section 3.4), and (2) a combined absolute magnitude M_V consistent with the system's observed *V* magnitude, distance, and extinction (see Table 7). The Aa component's physical parameters, which were used to generate test points, were obtained from Simón-Díaz et al. (2011), who used the NLTE FASTWIND code to model the star's spectrum. While they did not account for contributions from the other two stars, their results were primarily sensitive to the strength of He II lines, which should not be affected by Ab and C.

The bolometric luminosity contributions of the three components derived from their mass ratios are 90 per cent for Aa, 1 per cent for Ab, and 9 per cent for C. As a sanity check, evaluation of the Planck function for the inferred effective temperatures of the three components indicates that the fractional flux contribution of the C component in the *H* and *K* bands should be around 20 per cent, agreeing well with the interferometric results (Section 3.4).

Solving the projected masses for Aab (Table 3) using the masses inferred from the HRD yields $i_{\rm orb,\,Aab} = 72^\circ \pm 9^\circ$ using $(M_{\rm Aa} + M_{\rm Ab})\sin^3 i$, $i_{\rm orb,\,Aa} = 72^\circ \pm 6^\circ$ using $M_{\rm Aa}\sin^3 i$, and $i_{\rm orb,\,Ab} = 74^\circ \pm 24^\circ$ using $M_{\rm Ab}\sin^3 i$, i.e. consistent with the orbital inclination of the AC subsystem determined by interferometry. This suggests that the orbital axes of the Aab and AC subsystems are aligned. The masses of C and Aab, respectively 7.8 ± 0.7 and $18.8 \pm 1.2\,{\rm M_\odot}$, are consistent with the interferometric masses, albeit more precise by a factor of about 3 (although these results are more strongly model dependent).

Hut (1981) showed that the time-scales for spin–orbit alignment and pseudo-synchronization should be comparable, and much less than the time-scale for circularization. There is no evidence for synchronization of the orbital and rotational periods of NU Ori C, which is consistent with its wide and eccentric orbit. As shown below in Section 5.2, the orbital and rotational axes of NU Ori C are most likely misaligned.

The Aab orbit is nearly circular, and therefore may be expected to exhibit synchronized orbital and rotational motion and aligned orbital and rotational axes. Given the high $v\sin i$ of Aa, it is impossible for the rotational and orbital periods to be perfectly synchronized, since the maximum rotation period (if the rotational axis is exactly perpendicular to the line of sight) is 1.36 ± 0.15 d, much less than the 14.3 d orbital period. Assuming spin–orbit alignment and adopting $i_{\rm rot} = 70^\circ$ yields $P_{\rm rot} = 1.27 \pm 0.14$ d. This is very close to 1/11th of the orbital period, and could indicate a spin–orbit resonance. Assuming spin–orbit alignment for Ab yields $P_{\rm rot} = 10 \pm 6$ d, which is compatible (within the large uncertainty) with perfectly synchronized rotation, or with a rotation period of 1/2 or 1/3rd of the orbital period. While the rotational properties of

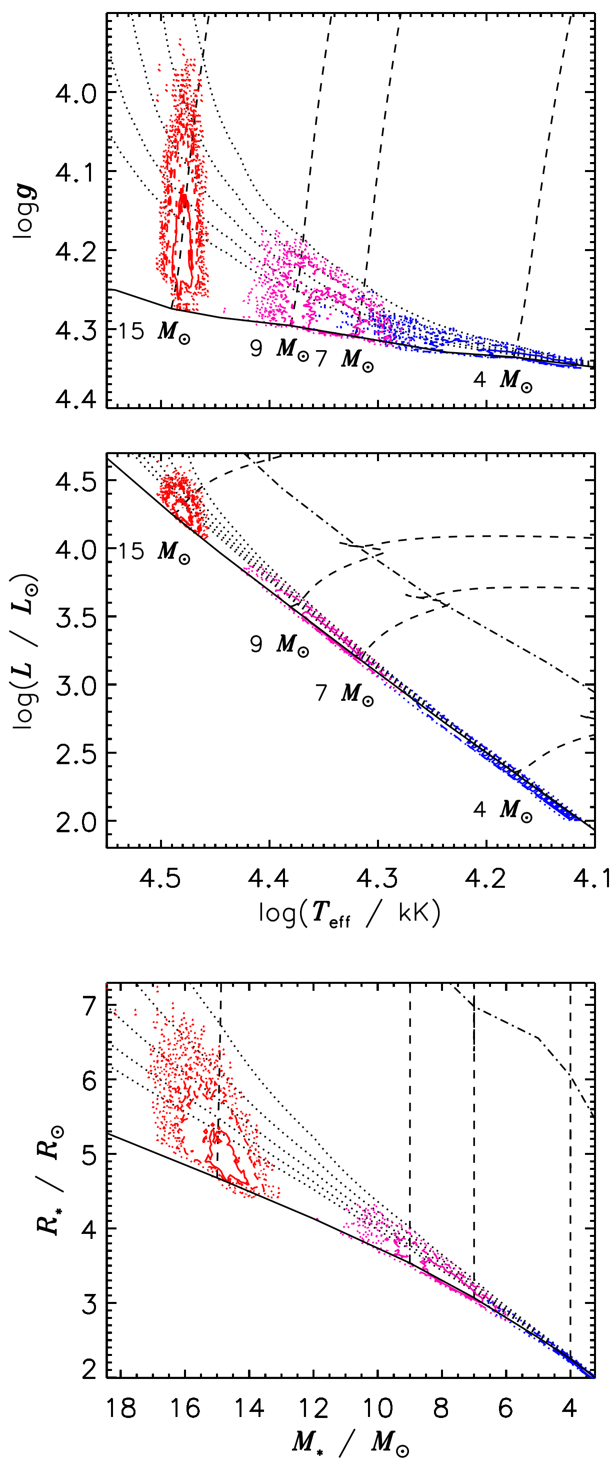

Figure 11. Stellar parameters of the components from Monte Carlo modelling. Contours indicate test point density (solid/dashed/dotted: $1\sigma/2\sigma/3\sigma$), with red, purple, and blue indicating Aa, C, and Ab. Dashed lines indicate evolutionary tracks from the rotating Ekström et al. (2012) models. Solid and dot–dashed lines show the zero-age and terminal-age main sequences. Dotted lines indicate isochrones from log (t/yr) = 6.5 to 6.9 in increments of 0.1.

Table 7. Stellar, rotational, magnetic, and magnetospheric parameters of the NU Ori components. Parameters obtained from the literature are indicated with superscripts corresponding to the following reference key: [a]Petit et al. (2013); [b]Simón-Díaz et al. (2011); and [c]Fukui et al. (2018). Surface magnetic dipole strengths for Aa and Ab correspond to 1σ/2σ/3σ upper limits (see text).

Parameter	Aa	Ab	C
V (mag)		6.83	
d (pc)		370 ± 30	
A_V (mag)		2.08 ± 0.25[a]	
M_V (mag)	−3.1 ± 0.2	0.1 ± 0.4	−1.5 ± 0.2
BC (mag)	−2.92 ± 0.03	−1.3 ± 0.2	−2.2 ± 0.1
$M_{\rm bol}$ (mag)	−6.2 ± 0.2	−2.0 ± 0.7	−4.3 ± 0.7
log (L/L$_\odot$)	4.29 ± 0.09	2.4 ± 0.3	3.3 ± 0.2
$T_{\rm eff}$ (kK)	30.5 ± 0.5[b]	15.2 ± 1.4	22.2 ± 1.0
log g	4.2 ± 0.1[b]	4.33 ± 0.01	4.28 ± 0.02
log ($t_{\rm cl}$/Myr)		5.75 ± 0.25[c]	
log ($t_{\rm HRD}$/Myr)		6.5 ± 0.2	
M_* (M$_\odot$)	14.9 ± 0.5	3.9 ± 0.7	7.8 ± 0.7
R_* (R$_\odot$)	5.1 ± 0.3	2.2 ± 0.2	3.3 ± 0.2
$v\sin i$ (km s^{-1})	190 ± 10	10 ± 5	100 ± 10
$v_{\rm mac}$ (km s^{-1})	20 ± 10	5 ± 5	5 ± 5
$P_{\rm rot}$ (d)	0.5–1.5	0.3–12.6	1.09478(7)
T_0	–	–	245 5222.2(1)
$v_{\rm eq}$ (km s^{-1})	–	–	175 ± 25
$R_{\rm K}$ (R_*)	–	–	2.6 ± 0.1
$i_{\rm rot}$ (°)	–	–	38 ± 5
β (°)	–	–	62 ± 6
$B_{\rm d}$ (kG)	<0.23/0.49/0.95	<0.1/0.6/6.0	7.9 ± 1.5
$R_{\rm A}$ (R_*)	–	–	18^{+5}_{-1}
log $R_{\rm A}/R_{\rm K}$	–	–	$0.84^{+0.09}_{-0.03}$

the Aab components are compatible with both spin–orbit alignment and pseudo-synchronization, this obviously cannot be confirmed. Given the system's youth (about 500 kyr; Fukui et al. 2018), there has not been much time for orbital evolution, and it may also be that it was born close to its current circular configuration. Alternatively, dynamical interactions with the C component may have circularized and hardened the Aab subsystem's orbit (Mazeh & Shaham 1979).

5.2 Magnetic field and magnetosphere of NU Ori C

To model the surface magnetic field of the C component, we utilized the sinusoidal fit to the $\langle B_z\rangle$ curve and the fit uncertainties (see Fig. 10) to solve Preston's equations for a centred, tilted dipole (Preston 1967). The rotational inclination $i_{\rm rot} = 38° \pm 5°$ was obtained from the R_*, $v\sin i$, and $P_{\rm rot}$ as $\sin i = v\sin i/v_{\rm eq} = v\sin i\, P_{\rm rot}/(2\pi R_*)$. The rotational inclination is clearly different from the interferometric orbital inclination. As noted above, spin–orbit misalignment is not surprising given the youth of the system and its wide, eccentric orbit.

The obliquity $\beta = 62° \pm 6°$ was determined from i and the sinusoidal fitting parameters from equation (2) using the Preston r parameter (Preston 1967):

$$r = \frac{|B_0| - B_1}{|B_0| + B_1}, \tag{3}$$

with β then given by (Preston 1967)

$$\beta = \tan^{-1}\left(\frac{1-r}{1+r}\frac{1}{\tan(i_{\rm rot})}\right). \tag{4}$$

The surface polar strength of the magnetic dipole $B_{\rm d} = 7.9 \pm 1.5$ kG was calculated using (Preston 1967)

$$B_{\rm d} = |\langle B_z\rangle|_{\rm max}\frac{20(3-\epsilon)}{15+\epsilon}\frac{1}{(\cos\beta\cos i_{\rm rot} + \sin\beta\sin i_{\rm rot})}, \tag{5}$$

with $|\langle B_z\rangle|_{\rm max} = |B_0| + |B_1|$ and the linear limb darkening parameter $\varepsilon = 0.38 \pm 0.02$ obtained from Díaz-Cordovés, Claret & Giménez (1995) for the $T_{\rm eff}$ and surface gravity inferred for NU Ori C from the HRD.

Shultz et al. (2017) noted that the stellar and magnetic parameters of NU Ori were very similar to those of ξ^1 CMa, making the failure to detect magnetospheric emission of a comparable strength in this star something of a mystery. This is partly resolved by the fact that it is NU Ori C, rather than NU Ori Aa, that is magnetic; thus, its stellar parameters are in fact *not* similar to those of ξ^1 CMa. However, the rapid rotation and strong magnetic field of NU Ori C still suggest that it may possess the ingredients necessary for a magnetosphere. The star's Kepler corotation radius $R_{\rm K}$ (equation 12; Townsend & Owocki 2005) is $2.6 \pm 0.1\ R_*$. To determine the system's Alfvén radius $R_{\rm A}$, or the furthest extent of closed magnetic loops within the magnetosphere, we used the Vink, de Koter & Lamers (2001) mass-loss rate and wind terminal velocity inferred from the star's physical parameters, obtaining $\log(\dot{M}/{\rm M_\odot\,yr^{-1}}) = -9.3^{+0.08}_{-0.4}$ and $v_\infty = 1200^{+1300}_{-100}$ km s^{-1}(where the asymmetric error bars reflect the bistability jump at the star's $T_{\rm eff}$). We then obtain $R_{\rm A} = 18^{+5}_{-1}\ R_*$ (equation 7; ud-Doula, Owocki & Townsend 2008), thus yielding a logarithmic ratio of $\log(R_{\rm A}/R_{\rm K}) = 0.84^{+0.09}_{-0.03}$.

These magnetospheric parameters are within the centrifugal magnetosphere (CM) regime identified by Petit et al. (2013) as correlated to the presence of Hα emission in many other magnetic early B-type stars. Inside a CM, rotational support of rigidly corotating, magnetically confined plasma prevents gravitational infall, enabling it to build-up to sufficiently high densities to be detectable in the Hα line. The emission signature of a CM is quite distinctive: typically, there are two emission bumps at high velocities (three or four times $v\sin i$), with no emission inside this range (e.g. Bohlender & Monin 2011; Grunhut et al. 2012; Oksala et al. 2012; Rivinius et al. 2013; Sikora et al. 2015). These arise due to the inability of plasma to accumulate below $R_{\rm K}$, where the centrifugal force is weaker than gravity (Townsend & Owocki 2005).

Emission strengths of CM stars are typically weak, around 10 per cent of the continuum or less. Given the flux contrast between NU Ori C and NU Ori Aa, we would then expect emission to be present at about the 1 per cent level. To see if such emission can be detected, synthetic line profiles were calculated using NLTE TLUSTY spectra from the BSTAR2006 library (Lanz & Hubeny 2007), interpolated to the inferred stellar parameters, convolved with the rotational velocities, shifted to the RVs, and combined using the inferred radii of the three components. Since the emission should be much stronger in Hα than in Hβ, synthetic profiles were created for both of these lines. Comparisons are shown in Fig. 12, where the six spectra with minimal contamination by telluric features were selected.

The fit within $\pm v\sin i$ of the Aa component is only approximate, likely due to factors unaccounted for in the model. The fit in the vicinity of the C II lines near 658 nm is poor, which likely explains the apparent emission excess in the red wing of Hα. The lack of variability in the red wing further suggests that the flux excess is spurious. However, in the blue wing there is a small amount of excess flux, on the order of 1 per cent of the continuum, which appears in some but not in all observations. According to the VALD line lists used to extract LSD profiles, there are no spectral lines in

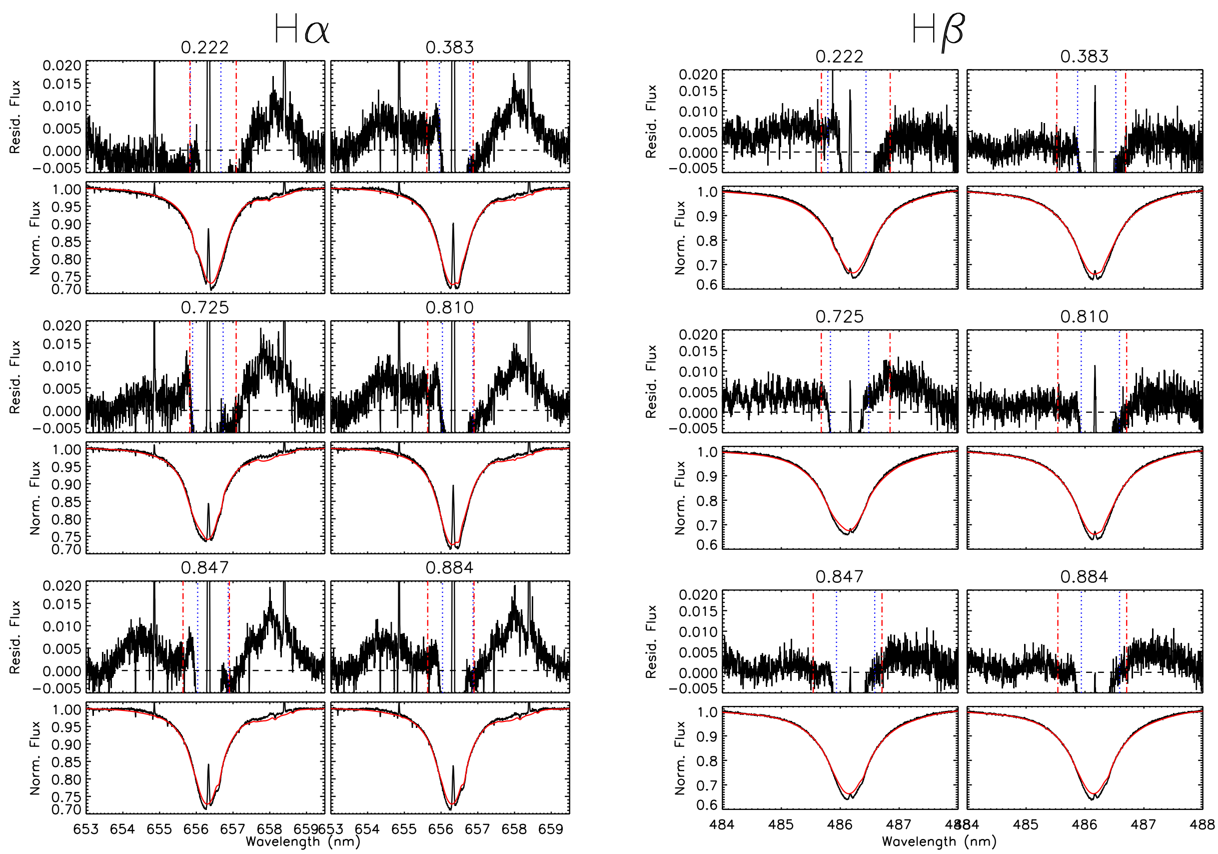

Figure 12. Left-hand panels: model fits to Hα (bottom panels) and residual flux (top panels). In the bottom panels, observed flux is shown in black, synthetic line profiles in red. In the top panels, the vertical blue dotted lines show $\pm v\sin i$ of NU Ori Aa, adjusted to the star's RV; red dot–dashed lines show $\pm R_{\rm K}$, adjusted to NU Ori C's RV; the horizontal dashed line indicates the continuum. Note the slight flux excess in the profile wings. Plot titles indicate rotational phases. Right-hand panels: as left-hand panels, bur for Hβ. Note the absence of excess flux at high velocity.

this region. This flux excess is located outside NU Ori C's Kepler radius, as expected for magnetospheric emission. However, the flux excess extends to $\sim 10\,R_{\rm C}$, which is significantly further than the $\sim 6\,R_*$ that is usually seen (e.g. Grunhut et al. 2012; Oksala et al. 2012; Rivinius et al. 2013). In contrast to H α, the wings of H β are essentially flat, again as expected for magnetospheric emission.

CM variability generally shows a characteristic rotationally coherent pattern of variability. Unfortunately, of the six observations of sufficient quality, four were obtained at similar phases (see plot titles in Fig. 12), making it impossible to say whether there is coherent variability following the expected pattern. Since only one magnetic pole is unambiguously seen in the $\langle B_z\rangle$ curve (Fig. 10), the emission strength of Hα should show only a single maximum, which should coincide with maximum $\langle B_z\rangle$ at phase 0; at phase 0.5, emission strength should be at a minimum. If the flux excess in the blue wing is real, the observations acquired near phases 0.2 and 0.8 should be the strongest, while those acquired near phases 0.4 and 0.7 should be the weakest. Instead, there is no flux excess at phase 0.2, and the flux excess at 0.4 is similar to that at 0.8. This discrepancy suggests that the blue flux excess is likely also spurious.

X-rays provide a reliable magnetospheric diagnostic, as magnetic B-type stars are typically overluminous in X-rays and generally exhibit harder X-ray spectra than non-magnetic stars (Nazé et al. 2014). NU Ori is an apparent exception to this rule, as its X-ray spectra are actually quite soft in comparison to other magnetic early-type stars (Stelzer et al. 2005; Nazé et al. 2014). Nazé et al. (2014) determined the star's X-ray luminosity, corrected for absorption by the interstellar medium, via four-temperature fits to the available *XMM–Newton* and *Chandra* data, finding $\log L_{\rm X} = 30.7 \pm 0.09$ erg s^{-1}. This agreed well with the prediction from the X-ray Analytic Dynamical Magnetosphere (XADM) model (ud-Doula et al. 2014), which they calculated under the assumption that the Aa component was magnetic, i.e. that the star was hotter, more luminous, and less strongly magnetized than is in fact the case.

Using the stellar and magnetic parameters for the C component, XADM predicts an X-ray luminosity of $\log L_{\rm X} = 29.9$, i.e. the star is overluminous by about 0.8 dex. This is similar to what has been observed for other rapidly rotating, strongly magnetized early B-type stars, e.g. σ Ori E, HR 5907, HR 7355, and HR 2949 (Nazé et al. 2014; Fletcher et al. 2017), all of which are overluminous by 1–2 dex. This may reflect enhanced X-ray production due to centrifugal acceleration of the plasma confined in the outermost magnetosphere (Townsend, Owocki & Ud-Doula 2007). Whether NU Ori's soft X-ray spectrum is anomalous in the context of X-ray overluminosity is inconclusive: while HR 5907 and HR 7355 both possess extremely hard X-ray spectra, σ Ori E's is relatively soft (Nazé et al. 2014). However, it should be emphasized that conclusions regarding luminosity and hardness are preliminary, as the X-ray spectra should first be corrected for the likely considerable contribution from the wind of the non-magnetic primary.

5.3 Magnetic fields of NU Ori Aa and Ab

While no magnetic field is detected in either Aa or Ab, the magnetic measurements obtained here can be used to establish upper limits on their surface magnetic field strengths. This would usually be accomplished by means of direct modelling of their Stokes V profiles, e.g. using a Bayesian inference approach (Petit & Wade 2012). However, given the likelihood that NU Ori C's contribution to Stokes V is still affecting the LSD profiles of Aa and Ab, this method cannot be utilized.

Instead, we adopt a novel method of establishing upper limits on $B_{\rm d}$, using $\langle B_z\rangle$ periodograms. The assumption is that there is no signal in either the Aa or Ab time series, and that the amplitudes of their respective periodograms thus provide a reasonable approximation of the maximum $\langle B_z\rangle$ amplitude that can be hidden in the noise at any given period. Since in both cases $v\sin i$ and R_* are known, the rotational inclination can be determined directly from the period. The periodogram is automatically limited at the upper end by taking the equatorial velocity to be the same as $v\sin i$, and at the lower end by the breakup velocity. In calculating the breakup velocity (and the inclination) we accounted for the rotational oblateness using the usual relationship for a rotating self-gravitating body (e.g. Jeans 1928). The obliquity is then determined from equations (3) and (4), with B_1 as the periodogram amplitude and B_0 fixed to 1 G (strictly speaking, for a pure noise $\langle B_z\rangle$ time series the mean value of $\langle B_z\rangle$ should be zero; however, if this is used, then $\beta = 90^\circ$ for all i and the parameter space is poorly explored). $B_{\rm d}$ is then determined as a function of i from equation (5), with $|\langle B_z\rangle|_{\rm max} = |B_0| + |B_1|$. Overall upper limits on $B_{\rm d}$ are then determined by marginalizing the resulting $B_{\rm d}$ distribution over i, under the assumption that $P(i) = 0.5\sin i$ (as is expected and generally observed; e.g. Abt 2001; Jackson & Jeffries 2010).

The results of this method are shown in Figs 13 and 14 for Aa and Ab, respectively. While the amplitude is relatively constant across the period ranges in question, the nature of Preston's relation leads to the inferred $B_{\rm d}$ values blowing up close to $i = 0^\circ$ or 90°. For Aa this is mitigated by the star's high $v\sin i$, which means that i cannot be smaller than about 15°. After marginalizing the distribution over i, the 1σ, 2σ, and 3σ upper limits for Aa are, respectively, 230, 490, and 950 G. The corresponding upper limits for Ab are 100, 600, and 6000 G, with the more extended low-probability tail arising due to the star's effectively unconstrained inclination.

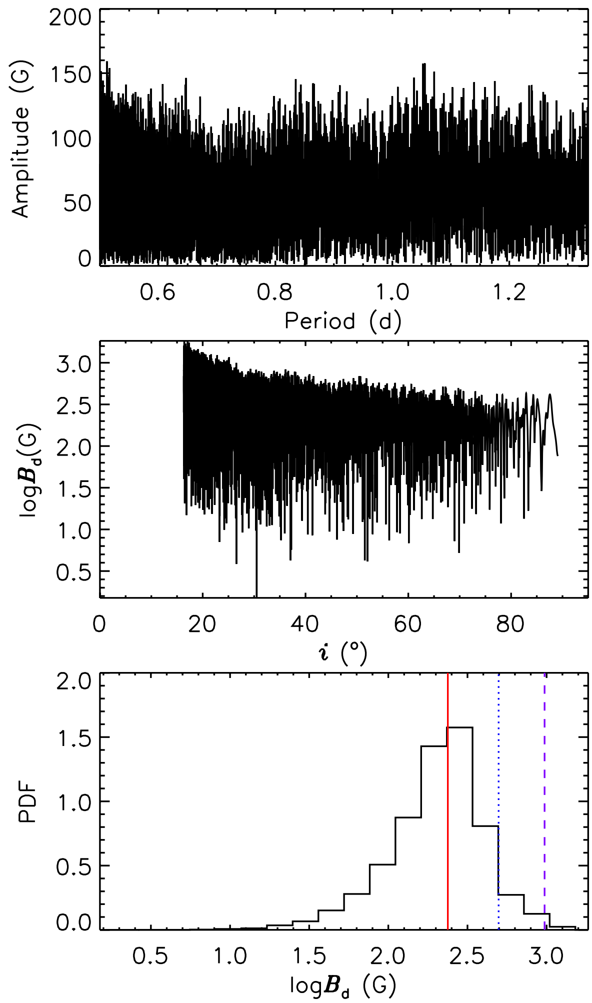

Figure 13. Illustration of the use of the $\langle B_z\rangle$ periodogram (for the measurements from the 30 kK LSD profiles) to obtain upper limits on $B_{\rm d}$ for NU Ori Aa. Top: the $\langle B_z\rangle$ periodogram, limited to the minimum and maximum periods from the star's rotational properties. The star's high $v\sin i$ indicates that i cannot be smaller than about 15°. Middle: $B_{\rm d}$ as a function of i, from converting the $\langle B_z\rangle$ periodogram into i and $B_{\rm d}$ using the star's rotational properties and Preston's relations. Bottom: PDF of $B_{\rm d}$ after marginalizing over i. The solid red, dotted blue, and dashed purple lines indicate 1σ, 2σ, and 3σ upper limits.

6 CONCLUSIONS

The line profile variability of NU Ori, seen especially in He I lines, can be explained by the contribution of a third star, which is also clearly detected in all interferometric observation; thus, NU Ori is an SB3 rather than an SB2. Measurement of the RVs of the three components via line profile fitting strongly suggest that they form a hierarchical triple: an inner system (Aab) composed of a 15 $M_\odot$ primary and a 4 $M_\odot$ secondary with an orbit of approximately 14 d, which is in turn orbited by an 8 $M_\odot$ tertiary (C) with an orbital period of about 476 d. Orbital modelling of RVs and interferometry indicates that the inner system is approximately circular, while the outer orbit is mildly eccentric. The orbital axes appear to be approximately aligned: the inclination of the orbital axis of AC, as determined via interferometry, is 70°.1 ± 0°.9, and the projected mass function for the inner binary yields 70° ± 4° based on the masses inferred from the HRD.

In principle, highly precise masses for the three stars can be obtained via interferometry. Unfortunately, the distance is not known with sufficient precision. Future *Gaia* data releases that account for multiplicity should yield a more accurate parallax for this system, with which a more precise comparison can be made between the astrometric masses and the masses inferred from evolutionary models. These data will also enable the orbital properties of the system to be further constrained.

We have found that the previously reported magnetic field, which had been attributed to the B0.5 V primary, is in fact hosted by the B2 V C component. This is supported by the confinement of the Zeeman signature within the line profile of the C component, and the movement of the Zeeman signature with the RV of the C rather than the Aa component. This has motivated a reanalysis of the rotational and magnetic properties of NU Ori. The previously reported rotational period of ∼1.1 d is confirmed, however, the inferred surface magnetic dipole strength is much stronger, about 8 kG. The rotational axis of the C component appears to be misaligned by about 30° relative to the AC orbital axis.

NU Ori C's rapid rotation and strong magnetic confinement are consistent with parameters typically associated with Hα emission, which would be expected at about 1 per cent of the continuum level of the SB3 system. We find evidence of emission at the expected

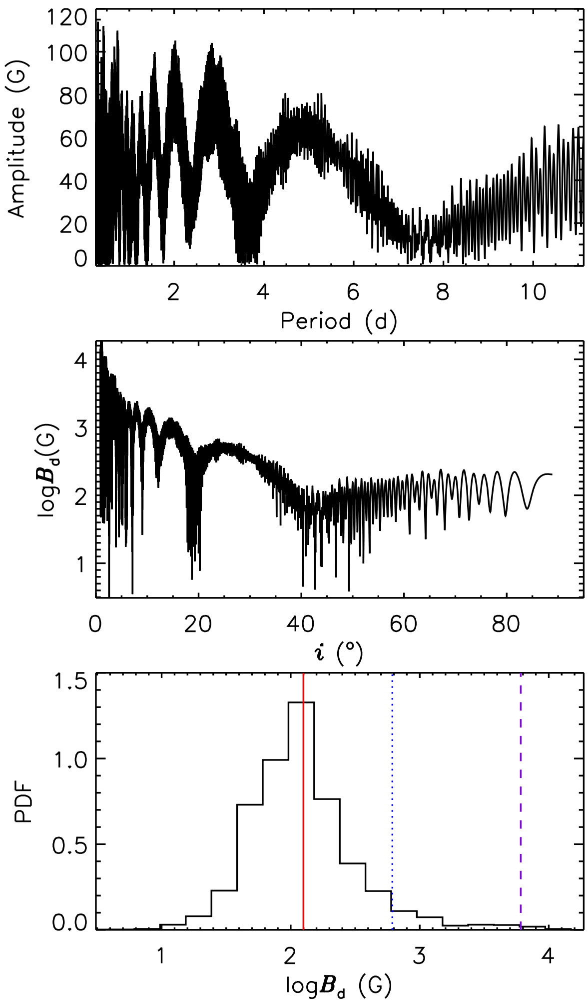

Figure 14. As Fig. 13, but for NU Ori Ab. The star's low $v\sin i$ means that i can be very small, leading to potentially very high values of $B_{\rm d}$.

magnitude via comparison of synthetic line profiles to Hα and Hβ observations, although this will need to be confirmed. Reevaluation of the star's expected X-ray luminosity shows that the system may show a degree of overluminosity similar to that of other rapidly rotating, strongly magnetic σ Ori E-type stars. This preliminary conclusion should be revisited by correcting the X-ray spectra for the influence of the non-magnetic primary, and isolating the X-ray spectrum of NU Ori C.

The 3σ upper limits on the surface dipole magnetic fields of the Aa and Ab components are about 1 and 6 kG, respectively (i.e. both stars are less, and probably much less, magnetic than NU Ori C), where we utilized a novel analytic method that combines rotational information to convert period spectra obtained from $\langle B_z \rangle$ time series into probability density functions of $B_{\rm d}$ marginalized over i.

ACKNOWLEDGEMENTS

This work has made use of the VALD data base, operated at Uppsala University, the Institute of Astronomy RAS in Moscow, and the University of Vienna. This work is based on observations obtained at the Canada–France–Hawaii Telescope (CFHT) that is operated by the National Research Council of Canada, the Institut National des Sciences de l'Univers of the Centre National de la Recherche Scientifique of France, and the University of Hawaii. This work is also based on observations collected at the European Organisation for Astronomical Research in the Southern Hemisphere under ESO programmes 60.A-0209(A), 092.C-0542(A), 094.C-0175(A), 094.C-0397(A), 096.D-0518(A), and 0100.C-0597(A). This work has made use of data from the European Space Agency (ESA) mission *Gaia* (https://www.cosmos.esa.int/gaia), processed by the *Gaia* Data Processing and Analysis Consortium (DPAC; https://www.cosmos.esa.int/web/gaia/dpac/consortium). Funding for the DPAC has been provided by national institutions, in particular the institutions participating in the *Gaia* Multilateral Agreement. This work utilized data obtained with GRAVITY. GRAVITY is developed in collaboration by the Max Planck Institute for Extraterrestrial Physics, LESIA of Paris Observatory/CNRS/UPMC/University of Paris Diderot and IPAG Université Grenoble, the Max Planck Institute for Astronomy, the University of Cologne, and the Centro Multidisciplinar de Astrofísica Lisbon and Porto. This project used the facilities of SIMBAD. All authors acknowledge the advice and assistance provided on this and related projects by the members of the BinaMIcS and MiMeS collaborations. MS acknowledges the support of the Annie Jump Cannon Fellowship endowed by the Mount Cuba Astronomical Observatory, and of the Natural Sciences and Engineering Research Council (NSERC) Postdoctoral Fellowship program. GAW acknowledges support from an NSERC Discovery Grant. OK acknowledges financial support from the Knut and Alice Wallenberg Foundation, the Swedish Research Council, and the Swedish National Space Board. PG acknowledges support from FCT-Portugal with reference UID-FIS-00099-2013.

REFERENCES

Abt H. A., 2001, AJ, 122, 2008
Abt H. A., Wang R., Cardona O., 1991, ApJ, 367, 155
Alecian E. et al., 2015, in Meynet G., Georgy C., Groh J., Stee P., eds, Proc. IAU Symp. Vol. 307, New Windows on Massive Stars: Asteroseismology, Interferometry, and Spectropolarimetry. Cambridge Univ. Press, Cambridge, p. 330
Babel J., Montmerle T., 1997, ApJ, 485, L29
Bohlender D. A., Monin D., 2011, AJ, 141, 169
Bonnell I. A., Bate M. R., 1994, MNRAS, 271, 999
Commerçon B., Hennebelle P., Henning T., 2011, ApJ, 742, L9
Díaz-Cordovés J., Claret A., Giménez A., 1995, A&AS, 110, 329
Donati J.-F., Semel M., Rees D. E., 1992, A&A, 265, 669
Donati J.-F., Semel M., Carter B. D., Rees D. E., Collier Cameron A., 1997, MNRAS, 291, 658
Donati J.-F. et al., 2006, MNRAS, 370, 629
Ekström S. et al., 2012, A&A, 537, A146
Fletcher C. L. et al., 2017, in Eldridge J. J., Bray J. C., McClelland L. A. S., Xiao L., eds, Proc. IAU Symp. Vol. 329, The Lives and Death-Throes of Massive Stars. Cambridge Univ. Press, Cambridge, p. 369
Fukui Y. et al., 2018, ApJ, 859, 166
Gaia Collaboration et al., 2016, A&A, 595, A2
Gaia Collaboration et al., 2018, A&A, 616, A1
Gelman A., Rubin D. B., 1992, Stat. Sci., 7, 457
González J. F., Levato H., 2006, A&A, 448, 283
Gravity Collaboration et al., 2017, A&A, 602, A94
Gravity Collaboration, Pfuhl O., Karl M., 2018, preprint (arXiv:1809.10376)
Grellmann R., Preibisch T., Ratzka T., Kraus S., Helminiak K. G., Zinnecker H., 2013, A&A, 550, A82
Grunhut J. H. et al., 2012, MNRAS, 419, 1610
Grunhut J. H. et al., 2017, MNRAS, 465, 2432
Hut P., 1981, A&A, 99, 126
Jackson R. J., Jeffries R. D., 2010, MNRAS, 402, 1380
Jeans J. H., 1928, Astronomy and Cosmogony. Cambridge Univ. Press, Cambridge

Köhler R., Petr-Gotzens M. G., McCaughrean M. J., Bouvier J., Duchêne G., Quirrenbach A., Zinnecker H., 2006, A&A, 458, 461
Kounkel M., 2017, PhD thesis, Univ. Michigan, Ann Arbor, MI
Kupka F. G., Piskunov N., Ryabchikova T. A., Stempels H. C., Weiss W. W., 1999, A&AS, 138, 119
Kupka F. G., Ryabchikova T. A., Piskunov N. E., Stempels H. C., Weiss W. W., 2000, Balt. Astron., 9, 590
Lanz T., Hubeny I., 2007, ApJS, 169, 83
Le Bouquin J.-B. et al., 2011, A&A, 535, A67
Le Bouquin J.-B. et al., 2017, A&A, 601, A34
Lenz P., Breger M., 2005, Commun. Asteroseismol., 146, 53
Mathys G., 1989, Fundamentals Cosmic Phys., 13, 143
Mayne N. J., Naylor T., 2008, MNRAS, 386, 261
Mazeh T., Shaham J., 1979, A&A, 77, 145
Mérand A. et al., 2014, Proc. SPIE, 9146, 91460J
Morrell N., Levato H., 1991, ApJS, 75, 965
Nazé Y., Petit V., Rinbrand M., Cohen D., Owocki S., ud-Doula A., Wade G. A., 2014, ApJS, 215, 10
Oksala M. E., Wade G. A., Townsend R. H. D., Owocki S. P., Kochukhov O., Neiner C., Alecian E., Grunhut J., 2012, MNRAS, 419, 959
Petit V., Wade G. A., 2012, MNRAS, 420, 773
Petit V., Wade G. A., Drissen L., Montmerle T., Alecian E., 2008, MNRAS, 387, L23
Petit V. et al., 2013, MNRAS, 429, 398
Piskunov N. E., Kupka F., Ryabchikova T. A., Weiss W. W., Jeffery C. S., 1995, A&AS, 112, 525
Preston G. W., 1967, ApJ, 150, 547
Rivinius T., Townsend R. H. D., Kochukhov O., Štefl S., Baade D., Barrera L., Szeifert T., 2013, MNRAS, 429, 177
Ryabchikova T. A., Piskunov N. E., Kupka F., Weiss W. W., 1997, Balt. Astron., 6, 244
Ryabchikova T., Piskunov N., Kurucz R. L., Stempels H. C., Heiter U., Pakhomov Y., Barklem P. S., 2015, Phys. Scr., 90, 054005
Sandstrom K. M., Peek J. E. G., Bower G. C., Bolatto A. D., Plambeck R. L., 2007, ApJ, 667, 1161
Schneider F. R. N., Podsiadlowski P., Langer N., Castro N., Fossati L., 2016, MNRAS, 457, 2355
Shultz M. et al., 2015, MNRAS, 449, 3945
Shultz M., Wade G. A., Rivinius T., Neiner C., Henrichs H., Marcolino W. MiMeS Collaboration, 2017, MNRAS, 471, 2286
Shultz M., Rivinius T., Wade G. A., Alecian E., Petit V., 2018a, MNRAS, 475, 839
Shultz M. E. et al., 2018b, MNRAS, 475, 5144
Sikora J. et al., 2015, MNRAS, 451, 1928
Simón-Díaz S., Herrero A., 2014, A&A, 562, A135
Simón-Díaz S., García-Rojas J., Esteban C., Stasińska G., López-Sánchez A. R., Morisset C., 2011, A&A, 530, A57
Simón-Díaz S., Godart M., Castro N., Herrero A., Aerts C., Puls J., Telting J., Grassitelli L., 2017, A&A, 597, A22
Stelzer B., Flaccomio E., Montmerle T., Micela G., Sciortino S., Favata F., Preibisch T., Feigelson E. D., 2005, ApJS, 160, 557
Townsend R. H. D., Owocki S. P., 2005, MNRAS, 357, 251
Townsend R. H. D., Owocki S. P., Ud-Doula A., 2007, MNRAS, 382, 139
ud-Doula A., Owocki S. P., 2002, ApJ, 576, 413
ud-Doula A., Owocki S. P., Townsend R. H. D., 2008, MNRAS, 385, 97
ud-Doula A., Owocki S., Townsend R., Petit V., Cohen D., 2014, MNRAS, 441, 3600
Vink J. S., de Koter A., Lamers H. J. G. L. M., 2001, A&A, 369, 574
Wade G. A. et al., 2016, MNRAS, 456, 2
Yakunin I. et al., 2015, MNRAS, 447, 1418

This paper has been typeset from a TEX/LATEX file prepared by the author.